Liu *et al. Biochar* (2026) 8:124
https://doi.org/10.1007/s42773-026-00640-w

Biochar

ORIGINAL RESEARCH Open Access

Microwave-assisted β-cyclodextrin modified calcium-rich biochar for tetracycline removal from wastewater: mechanistic, machine learning, density functional theory calculations and life cycle assessment

Chong Liu[1,2], Grégorio Crini[3*], Ricardo Bello-Mendoza[4], Lee D. Wilson[5], Ali H. Jawad[6,7], Paramasivan Balasubramanian[8], Xuan Cuong Nguyen[9,10], Qingfu Zheng[11] and Fayong Li[1*]

Abstract

The removal of antibiotics from water using sustainable and cost-effective methods remains an environmental challenge. In this study, cotton-stalk biochar (CBC) was used as a substrate and waste eggshells as a calcium source to prepare a β-cyclodextrin-functionalized adsorbent (Ca@CBC/β-CD) via microwave-assisted crosslinking. The obtained material was used for tetracycline (TC) removal from water. Experimental results showed that Ca@CBC/β-CD exhibited the best adsorption performance at approximately pH = 6, and the adsorption kinetics were well described by the pseudo-second-order model. The adsorption isotherm followed the Langmuir model, with the maximum adsorption capacity increasing from 142.36 mg g^{-1} at 25 °C to 161.91 mg g^{-1} at 45 °C. The adsorbent also showed good tolerance to common coexisting ions and retained about 84–86% of its initial capacity after five regeneration cycles. Spectroscopic characterization combined with density functional theory (DFT) calculations revealed that TC adsorption was governed by the synergistic contribution of Ca^{2+} inner-sphere complexation/surface bridging, β-CD host–guest inclusion, and multi-point hydrogen bonding. Among the tested machine-learning models, the gradient boosting decision tree showed the best predictive performance (test-set $R^2 = 0.9914$) and identified initial concentration, adsorbent dosage, and contact time as the key adsorption factors. Life-cycle assessment further indicated that the preparation stage generated 5.44 kg CO_2-eq per kg adsorbent, with electricity being the primary hotspot. Overall, Ca@CBC/β-CD represents an efficient, reusable, and relatively sustainable adsorbent for TC removal from water.

Highlights

- A new adsorbent from waste cotton stalks and eggshells captures antibiotics through pores and surface sites.
- Tests and quantum-level calculations show efficient, reusable removal of antibiotics from water.

*Correspondence:
Grégorio Crini
gregorio.crini@univ-fcomte.fr
Fayong Li
lisen8279@163.com
Full list of author information is available at the end of the article

Springer

- A machine learning model accurately predicted adsorption performance and highlighted the most important factors.
- Life cycle assessment found electricity use is the main environmental hotspot in adsorbent production.

Keywords β-cyclodextrin, Biochar, Tetracycline, Machine learning, Adsorption, Life cycle assessment

Graphic Abstract

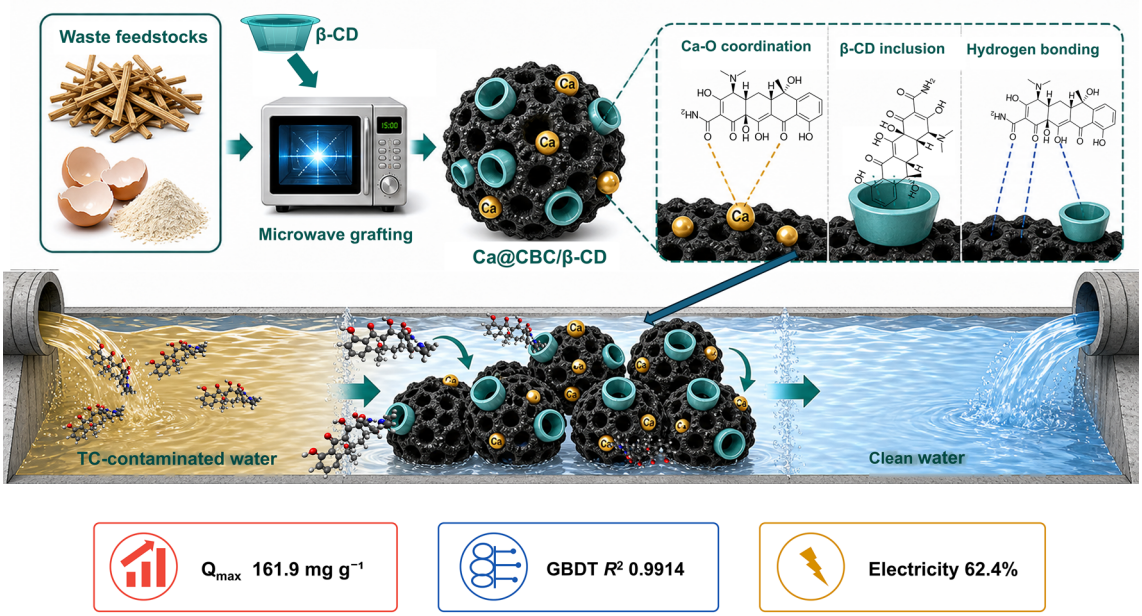

1 Introduction

Antibiotics are widely used in human and veterinary medicine, resulting in their pervasive occurrence across environmental matrices worldwide (Zhang et al. 2023a; Huang et al. 2023). Among them, tetracycline (TC), as a broad-spectrum antibiotic, has seen extensive application in livestock and aquaculture due to its low cost and high efficacy in treating bacterial infections (Nie et al. 2023; Zhang et al. 2023b). However, TC and its transformation products can be excreted directly through animal feces and urine, leading to contamination of surface water, groundwater, and soils (Zhang et al. 2023b; Li et al. 2025). Recently, Antos et al. reported that the average degree of TC contamination in European waters varied from 0 to 20 ng L^{-1} (Antos et al. 2024). It is therefore imperative to develop efficient and economical technologies for removing TC from aquatic environments. Current approaches for TC removal from wastewater include biodegradation, precipitation, ion exchange, solvent extraction, coagulation–flocculation, adsorption onto conventional adsorbents, biosorption onto innovative materials, chemical reduction, and advanced oxidation (Liao et al. 2022; Chen et al. 2023; Kayani 2025). Among these, adsorption is particularly attractive owing to its operational simplicity, low cost, low-energy requirements, high efficiency, and minimal risk of secondary pollution (Jiang et al. 2023). Despite extensive work on both conventional and unconventional adsorbents, the persistent need for materials that are highly effective, low-cost, naturally derived, easy to use, and environmentally benign continues to drive active research in this area.

Traditionally, activated carbons in both granular and powdered forms, derived from natural resources such as coconut shells, lignite, and wood, have been extensively investigated as efficient adsorbents because of their well-developed pore structure, high surface area, and simple operation. Compared with other adsorbents, such as activated alumina, they often exhibit superior removal performance (Sanni et al. 2024). However, their cost remains a significant drawback, and regeneration is complex.

Recent efforts have shifted toward economical biomass-derived sorbents such as biochar (Liu et al. 2024a, 2024b). The intrinsic adsorption capacity of raw biochar is nevertheless often limited, which has spurred broad interest in chemical and composite modification strategies (e.g., alkaline, acidic, metallic, organic, and hybrid modifications) (Xu et al. 2022). Calcium (Ca) modification is especially prevalent, as it is widely available from abundant, low-cost sources, such as bones and shells. Ca can generate CaO phases and develop microporosity during thermal treatment, substantially increasing specific surface area and micropore volume and thereby enhancing adsorption performance and techno-economic feasibility (Zhuo et al. 2022).

Nonetheless, Ca-modified biochar may still lack sufficient surface functional groups. It has been reported that macromolecular and oligomer modifiers, such as chitosan, sodium alginate, and cyclodextrins, could introduce additional binding sites (Khushbu 2022). Among them, cyclodextrins (CDs) are cyclic oligomers obtained from the enzymatic degradation of starch, composed of glucose units with a hydrophilic external surface and a hydrophobic internal cavity. CDs have attracted sustained interest because they are environmentally benign, readily available from renewable feedstocks, non-toxic, biocompatible, and biodegradable, while exhibiting strong affinity toward aqueous contaminants such as dyes, phenolic derivatives, pesticides, pharmaceuticals, endocrine-disrupting chemicals, and metals (Urooj et al. 2024; Liu et al. 2024c). In particular, β-cyclodextrin (β-CD), the most industrially produced and most used CD, has emerged as a versatile host motif for adsorbent design (Liu et al. 2024c; Tian et al. 2021). β-CD can enhance pollutant affinity via hydrophobic interactions due to its capacity to form an inclusion complex, while its abundant surface hydroxyls provide additional active sites (Liu et al. 2024c). For the functionalization step, microwave irradiation is advantageous over conventional external heating because it allows for rapid volumetric heating, shorter reaction time, and lower energy demand during β-CD grafting (Qu et al. 2022; Han 2025). Accordingly, in the present Ca@CBC/β-CD system, microwave treatment was adopted specifically to intensify the β-CD immobilization step, rather than the initial carbonization step, so as to improve grafting efficiency under a faster and more energy-efficient preparation route.

Furthermore, although conventional batch adsorption tests are standard, they are labor-intensive, time-consuming, and costly, and they provide limited insight into interactions among operating variables (Liu et al. 2025a). Data-driven machine learning (ML) can capture nonlinear relationships between inputs and responses (Liu et al. 2025b, 2025c). Although ML has been applied to biochar adsorption (Zhang et al. 2023b; Balasubramanian et al. 2024), studies focused specifically on TC uptake by Ca-modified biochar crosslinked with β-CD (Ca@CBC/β-CD), and on identifying the most influential parameters, remain scarce. Moreover, despite the strong adsorption afforded by some metal-modified biochar, their broader environmental implications have been underexamined. Integrating life-cycle assessment (LCA) to quantify environmental and human-health impacts of Ca@CBC/β-CD would provide critical evidence to support scale-up.

Therefore, this work aims to design and develop a β-CD-crosslinked, calcium-modified cotton-stalk biochar for efficient removal of TC from wastewater, and to evaluate its performance mechanistically and holistically using density functional theory (DFT) calculations, ML analysis, and LCA. The specific objectives are: (i) Synthesize and characterize a Ca@CBC/β-CD; (ii) Assess the adsorption performance of Ca@CBC/β-CD for TC and elucidate the underlying mechanisms; (iii) Conduct DFT simulations to clarify interactions between key TC functional groups and the Ca@CBC/β-CD surface; (iv) Apply ML models to analyze experimental data and identify the most influential experimental factors; (v) Develop a Python-based application that integrates the selected ML model to predict the adsorption performance of Ca@CBC/β-CD; (vi) Perform an LCA to evaluate the environmental impacts and sustainability of Ca@CBC/β-CD.

2 Materials and methods

2.1 Materials and synthesis of adsorbents

Cotton stalk powder was obtained from laboratory stock. Waste eggshells were collected from the dining facilities. β-cyclodextrin (≥ 98%, AR) and glutaraldehyde (AR) were procured from Tianjin Huasheng Chemical Reagent Co., Ltd. (Tianjin, China). Cotton stalks were freed of extraneous matter, thoroughly rinsed with deionized (DI) water, dried at 105 °C for 12 h, ground, and passed through a 60-mesh sieve. Similarly, the collected waste eggshells were manually stripped of the inner membrane, thoroughly washed with deionized water to remove residual impurities, dried at 105 °C, ground, and sieved to 60 mesh before use. This pretreatment was intended to minimize the influence of residual organic matter and particle-size variation on the subsequent carbonization process and on the consistency of the Ca source. The pretreated cotton-stalk powder was loaded into a quartz boat and placed in a tube furnace, purged with N_2 (200 mL min^{-1}) for 30 min, heated to 600 °C at 5 °C min^{-1}, and held for 3 h. The furnace was then allowed to cool to

room temperature under N_2. The product (cotton-stalk biochar) is hereafter denoted as CBC.

Eggshell powder and cotton stalk powder were blended at a 1:1 mass ratio. A small amount of DI water was nebulized over the mixture solely to suppress dust, followed by air-drying. The mixture was carbonized under N_2 using the same protocol as for CBC (200 mL min^{-1}; ramp 5 °C min^{-1} to 600 °C; hold 3 h), then cooled to room temperature to produce Ca@CBC.

The microwave-assisted β-CD functionalized carbon-based material approach adopted in this study is adapted from previously reported literature (Qu et al. 2020; de Benedicto et al. 2024). This route was selected because it enables the incorporation of waste-derived Ca mineral domains and β-CD interfacial functionality into a single adsorbent platform through rapid grafting. β-CD (2.0 g) and NaOH (3.5 g) were dissolved in water (50 mL). The target biochar (0.30 g; CBC or Ca@CBC) and glutaraldehyde (1 mL) were mixed; the suspension was dispersed thoroughly, and the mixture was subjected to microwave irradiation at 350 W for 15 min. The solid was collected by vacuum filtration, dried, and gently ground to yield the grafted powder. Samples derived from CBC are designated CBC/β-CD; those from Ca@CBC are designated Ca@CBC/β-CD.

2.2 Materials characterization

Elemental composition of the adsorbents was determined using an Elementar vario ISOTOPE select (Germany) analyzer. A Micromeritics ASAP 2460 apparatus was employed for Brunauer–Emmett–Teller (BET) specific surface area analysis. Sample morphology was examined by scanning electron microscopy (SEM) on a Thermo Fisher Scientific Apreo 2S + microscope, while energy-dispersive X-ray spectroscopy (EDS) was conducted using an Oxford Instruments Ultim Max 65 instrument. Crystal phase identification was performed using X-ray diffraction (XRD) with a Bruker D8 Advance (Germany) equipment, operated at 40 kV and 40 mA with Cu $K\alpha_1$ radiation (λ = 0.15406 nm) and a step size of 0.02. X-ray photoelectron spectroscopy (XPS) was performed using a Thermo Fisher Scientific ESCALAB 250Xi (USA) instrument. Fourier-transform Infrared (FT-IR) spectra were collected with a Thermo Scientific Nicolet iS5 apparatus.

2.3 Experimental procedures

All batch adsorption experiments were conducted using flasks with a working volume of 100 mL, placed in a thermostated orbital shaker (25 ± 1 °C, 150 rpm). Unless otherwise specified, the initial TC concentration (C_0) was 50 mg L^{-1} and the adsorbent dosage was 0.5 g L^{-1}. Solution pH was adjusted with 0.1 M HCl or NaOH. At the end of the contact time, suspensions were membrane-filtered, and the residual TC concentration was quantified by UV–Vis spectrophotometry at 360 nm. All measurements were performed in triplicate, and mean values are reported. Adsorption capacity (Q_e mg g^{-1}) and removal efficiency (R_{re}, %) were calculated according to Eqs. (1 , 2), respectively.

$$Q_e = \frac{(C_0 - C_e) * V}{m} \tag{1}$$

$$R_{re} = \frac{C_0 - C_e}{C_0} \times 100\% \tag{2}$$

where C_0 and C_e are the initial and equilibrium TC concentrations (mg L^{-1}), respectively, V is the volume of TC solutions (L), and m is the mass of the adsorbent (g).

Kinetic tests were carried out using Ca@CBC/β-CD as a representative sorbent at pH = 6.0, C_0 = 50 mg L^{-1}, dosage = 0.5 g L^{-1}, and 25 °C, with aliquots withdrawn over 0–300 min. The data were fitted by non-linear regression to pseudo-first-order and pseudo-second-order models, and intraparticle diffusion behavior was further analyzed. Equilibrium isotherms were obtained at pH = 6.0 and a dosage of 0.5 g L^{-1} by equilibrating TC solutions (25–350 mg L^{-1}) for 3 h at 25, 35, and 45 °C to determine Q_e. The resulting data were fitted to the Langmuir and the Freundlich models. Parameters, governing equations, and additional notes pertinent to adsorption kinetics, isotherms, and thermodynamics are summarized in Table S1.

Under the baseline adsorption conditions described above, the effects of coexisting species on the adsorption performance of Ca@CBC/β-CD were evaluated. The anions NO_3^-, SO_4^{2-}, CO_3^{2-}, and $H_2PO_4^-$, the cations K^+, Na^+, Mg^{2+}, and Ca^{2+}, as well as humic acid (HA) and the trivalent cations Fe^{3+} and Al^{3+}, were individually introduced at concentrations of 0, 50, and 100 mg L^{-1}. After 3 h of contact, the suspensions were filtered through a 0.45 μm membrane, and C_e and Q_e were determined to evaluate the effects of coexisting species and their concentrations (Shi et al. 2023). For regeneration, 0.1 M NaOH was used as the desorbent. Saturated sorbents were shaken in the alkaline solution for 12 h, rinsed with deionized water to neutrality, and reused in the subsequent cycle. The equilibrium uptake in each cycle (Q_e) was recorded to evaluate reusability. To assess Ca leaching, Ca@CBC/β-CD (0.5 g L^{-1}) was dispersed in deionized water adjusted to pH 6.0 at 25 ± 1 °C and 150 rpm. At selected time intervals, the supernatant was filtered through a 0.45 μm membrane, and the dissolved Ca^{2+} concentration was determined by ICP-OES.

2.4 Machine learning evaluation of experimental conditions

Building on the experimental results in Sect. 2.3, this study employed ML to (i) predict the Q_e under multifactorial conditions and (ii) quantify the relative influence and interactions among variables that are not captured by conventional kinetic/isotherm studies. ML is warranted because the adsorption response is highly nonlinear and multivariate. Parametric models (e.g., pseudo-first/second-order kinetics, Langmuir/Freundlich isotherms) describe single-factor trends but do not generalize across the full experimental design space or provide a principled ranking of factor importance.

This study evaluated six supervised algorithms: Random Forest (RF), Gradient-Boosted Decision Trees (GBDT), LightGBM (LGBM), CatBoost, Elastic Net (EN), and TabPFN. RF, GBDT, LGBM, and CatBoost—tree-based ensemble methods—were selected for their transparent structure, minimal feature preprocessing, and strong capacity to capture nonlinearities and higher-order interactions. EN (a penalized linear model) and TabPFN (a Transformer-based tabular predictor) served as non-tree baselines to benchmark performance and test the robustness of our conclusions. Algorithmic principles and key hyperparameters are summarized in Table S2. All raw data and analysis code are available on GitHub (see Data availability) to ensure reproducibility and transparency.

The dataset was partitioned into training and testing subsets at a 7:3 ratio. Bayesian optimization with five-fold cross-validation was used to identify optimal hyperparameters over the ranges shown in Table S2. Relative to grid-search cross-validation, Bayesian optimization reduces computational cost while exploring the hyperparameter space more efficiently, mitigating local optima and improving generalization and predictive accuracy. Model performance on both the training and testing sets was assessed using the root-mean-square error (RMSE) and the coefficient of determination (R^2), computed as in Eqs. (3–4) (Liu et al. 2024a):

$$\mathrm{RMSE} = \sqrt{\sum_{i=1}^{n} \frac{(y_i - x_i)^2}{n}} \tag{3}$$

$$R^2 = 1 - \frac{\sum_{i=1}^{n} (y_i - x_i)^2}{\sum_{i=1}^{n} (y_i - \overline{y_i})^2} \tag{4}$$

In these equations, y_i represents the predicted value, x_i the corresponding experimental measurement, and $\overline{y_i}$ the mean of all experimental data points.

To interpret the fitted models, this study conducted an analysis using Shapley Additive exPlanations (SHAP). SHAP values quantify the average impact of each feature on the prediction and attribute the contribution of specific feature values to individual outputs, which is particularly useful for elucidating the behavior of complex tree-based ensembles and identifying key drivers. Finally, this study implemented a Python-based graphical user interface (GUI) that integrates the selected model to evaluate the tetracycline adsorption performance of Ca@CBC/β-CD.

2.5 Density functional theory (DFT) calculations

All DFT calculations were run in Gaussian 09. Geometries and single point energies were calculated using the dispersion corrected ωB97X-D/def2-TZVP level with an UltraFine grid, Tight SCF, and quadratic convergence (XQC; up to 512 iterations). Opt = CalcFC was applied, and harmonic frequencies verified minima (no imaginary modes) and provided zero point and thermal corrections. Solvation was treated with the SMD model for water (SCRF = (SMD, Solvent = Water)). Intermolecular contacts were analyzed using the independent gradient model based on Hirshfeld partition (IGMH) and Hirshfeld surface (HS) analysis. IGMH (Multiwfn v3.9) defined adsorbate and substrate as fragments to compute the interfragment descriptor $\delta g^{\mathrm{inter}}$; fixed $\delta g^{\mathrm{inter}}$ isosurfaces

Table 1 Elemental composition and pore structure characteristics of various biochar and modified biochar materials

Material	Elemental composition[a]					Surface area and pore structure characteristics[b]		
	N (%)	C (%)	H (%)	S (%)	C/H	BET surface area ($m^2\ g^{-1}$)	Average pore diameter (nm)	Total pore volume ($cm^3\ g^{-1}$)
CBC	1.316	80.835	1.627	0.564	49.683	15.720	11.460	0.045
Ca@CBC	0.536	27.603	0.503	0.254	54.877	28.789	2.780	0.020
CBC/β-CD	1.295	82.159	1.653	0.337	49.703	44.312	8.667	0.096
Ca@CBC/β-CD	0.493	25.306	0.595	0.159	42.531	83.869	3.082	0.065

[a] Elemental analysis was performed using an elemental analyzer

[b] N_2 adsorption–desorption was carried out at −195.8 °C (analysis bath temperature)

colored by sign(λ_2)ρ identified attractive (blue), weak (green), and repulsive (red) regions, locating hydrogen bonds, π–π stacking, and metal–ligand interactions (Lu and Chen 2012; Lu 2024). HS maps (d_{norm}, shape index, and curvedness) and fingerprint plots (d_e vs d_i) quantified contributions of close contacts. Together, these results provide spatially resolved evidence for interfacial weak interactions, supporting the discussion of adsorption site selectivity and binding mechanisms.

2.6 Life cycle assessment

This study conducted an LCA of the Ca@CBC/β-CD for TC removal, aiming to quantify the environmental burden of the adsorbent preparation stage (Stage 1) to inform subsequent material optimization and scale-up. Following the workflow in Fig. S1, the system boundary was partitioned into three stages: Stage 1—raw-material inputs and adsorbent synthesis (Synthesis); Stage 2—adsorption use and regeneration (Adsorption & Regeneration); and Stage 3—end-of-life scenarios (End-of-life). Consistent with prior studies, the analysis was restricted to Stage 1 on a cradle-to-gate basis (Chen et al. 2024; Wang et al. 2024). Using LCA software (SimaPro 9.5), in conjunction with the ecoinvent v3.9.1 database, the LCA modeling adhered to the CML-IA baseline method.

The life cycle inventory (LCI) covers pyrolysis of cotton-stalk powder to produce CBC; use of waste eggshells as the Ca source, including CO_2 released upon decomposition; β-CD grafting and glutaraldehyde crosslinking; and consumption of NaOH, deionized water, nitrogen/steam, and electricity, together with the associated wastewater. For substances not present in the database (e.g., β-CD and glutaraldehyde), proxy processes were adopted or reconstructed from the literature, and ethanol recovery was represented as a negative input. Eggshells were modeled as post-consumer biowaste, with collection/transport and process emissions included. All inputs and emissions were normalized to a functional unit of 1 kg of adsorbent. Key parameters and data sources are summarized in Table S4.

3 Results and discussion

3.1 Materials' physicochemical properties

Table 1 summarizes the elemental compositions and textural parameters of the biochar and its modified derivatives. The pristine cotton-stalk biochar (CBC) shows a high carbon content (C = 80.835%) and a modest pore structure, with a BET specific surface area of 15.720 $m^2\ g^{-1}$, a total pore volume of 0.045 $cm^3\ g^{-1}$, and an average pore diameter of 11.460 nm. The incorporation of eggshell-derived Ca (Ca@CBC) lowers the carbon content to 27.603% and increases the surface area to 28.789 $m^2\ g^{-1}$. At the same time, the total pore volume decreases to 0.020 $cm^3\ g^{-1}$ and the average pore diameter shrinks to 2.780 nm, indicating the generation of more micropores. Grafting β-cyclodextrin onto CBC (CBC/β-CD) retains a high carbon content (82.159%), increases the surface area to 44.312 $m^2\ g^{-1}$, enlarges the pore volume to 0.096 $cm^3\ g^{-1}$, and reduces the average pore diameter to 8.667 nm, suggesting more accessible porosity. Subsequent β-CD grafting on Ca@CBC (Ca@CBC/β-CD) affords the highest surface area among the four materials (83.869 $m^2\ g^{-1}$), with a moderate pore volume (0.065 $cm^3\ g^{-1}$) and a small average pore diameter (3.082 nm), and a carbon content of 25.306%. Overall, Ca incorporation mainly promotes microporosity (higher surface area but smaller pore diameter and volume), whereas β-CD functionalization increases surface area and—when applied directly to CBC—markedly enlarges pore volume; combining Ca with β-CD maximizes surface area though not pore volume. In addition, the low but measurable N content of the materials listed in Table 1 mainly arises from the native N-containing constituents of the cotton stalk biomass, because no external N source was intentionally introduced during synthesis.

As shown in Fig. S2, the N_2 adsorption–desorption isotherm of Ca@CBC/β-CD reveals a hierarchical micro/mesoporous structure. The pronounced uptake at low P/P_0 indicates micropore filling, whereas the gradual increase at intermediate relative pressures and the final upturn near saturation suggest the additional presence of mesoporous and textural porosity (Qu et al. 2024). This agrees well with the textural parameters summarized in Table 1, including a BET surface area of 83.87 $m^2\ g^{-1}$, a total pore volume of 0.0646 $cm^3\ g^{-1}$, a t-plot micropore volume of 0.0222 $cm^3\ g^{-1}$, and a BJH average pore diameter of 6.16–7.00 nm, confirming that Ca@CBC/β-CD is dominated by small mesopores with a non-negligible microporous contribution. For clarity, the inset pore-size-distribution curve in Fig. S2 was restricted to the 0–50 nm range. The broad distribution observed within this interval further confirms the presence of a hierarchical pore network, which enhances both the accessibility of adsorption sites and the diffusion of TC molecules.

SEM imaging reveals pronounced changes in surface morphology across the materials (Fig. 1a–d). The pristine CBC (Fig. 1a) retains the elongated vascular pores characteristic of cotton stalk biomass; pore walls are relatively smooth with only minor residual mineral particulates. After co-carbonization with eggshells (Ca@CBC, Fig. 1b), the surface becomes markedly rough and densely populated with bright nano- to submicrometer particulates accompanied by numerous pits—features attributable to Ca-containing inorganic phases derived from the eggshell. β-Cyclodextrin grafting of CBC (CBC/β-CD, Fig. 1c) further increases surface roughness, with

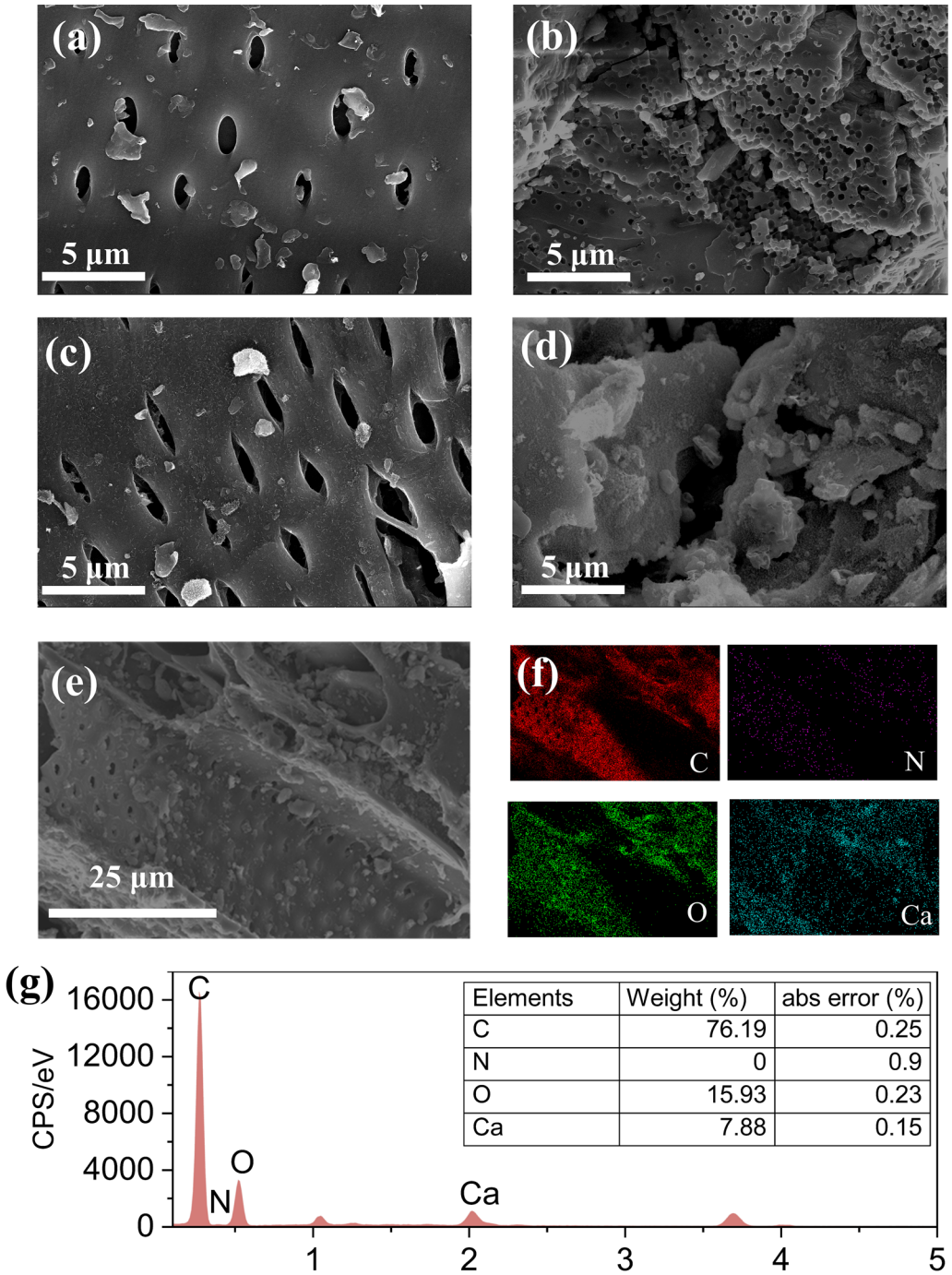

Fig. 1 The morphology and elemental distribution of the synthesized materials

some pore openings covered by lamellar or film-like deposits. Subsequent β-CD functionalization of Ca@CBC (Ca@CBC/β-CD, Fig. 1d) yields the most pronounced hierarchical architecture: a polymeric coating uniformly anchored on Ca-rich particulates generates abundant edge and defect sites that would be favorable for interfacial reactions and mass transfer.

Elemental mapping of Ca@CBC/β-CD (Fig. 1e, f) shows C as the dominant framework element, while O and Ca are uniformly distributed over the carbon matrix, indicating homogeneous fixation of Ca species. A weak

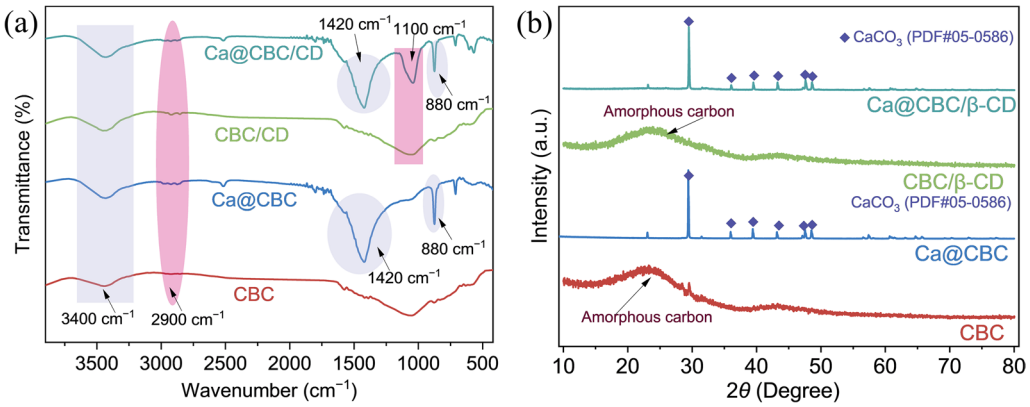

Fig. 2 **a** FT-IR and **b** XRD images of various biochar and modified biochar materials

N signal is also detected. The EDS spectrum (Fig. 1g) shows surface contents of 76.19 wt% C, 15.93 wt% O, and 7.88 wt% Ca. For comparison, SEM–EDS analysis of Ca@CBC before β-CD grafting (Fig. S3) gives 53.74 wt% C, 1.28 wt% N, 26.66 wt% O, and 18.32 wt% Ca. The reduced apparent surface Ca content after β-CD grafting is attributed to partial coverage of Ca-rich domains by the β-CD-derived organic coating, rather than loss of the Ca phase itself. Such structural evolution is directly responsible for the improved TC adsorption of Ca@CBC/β-CD. Specifically, the hierarchical micro/mesoporous structure and the highest BET surface area across the four materials facilitate TC transport to internal active sites, whereas the rough Ca-rich domains and oxygen-containing β-CD coating provide abundant accessible centers for Ca-mediated complexation/bridging, host–guest inclusion, and hydrogen bonding. These features collectively account for the enhanced TC uptake.

FT-IR spectra (Fig. 2a) capture the chemical changes induced by Ca and β-CD modification. CBC exhibits a broad band at ~ 3400 cm^{-1} (–OH stretching) and weak C–H absorptions near ~ 2900 cm^{-1}, typical of amorphous biochar. After co-carbonization with eggshells (Ca@CBC), new bands emerge at ~ 1420 and ~ 880 cm^{-1}, assigned to the ν_3 and ν_2 modes of CO_3^{2-}, confirming the formation/retention of $CaCO_3$ at 600 °C. Following β-CD grafting, the –OH region (~ 3400 cm^{-1}) intensifies, and the C–O/C–O–C vibrations at 1100 cm^{-1} are markedly enhanced, consistent with glycosidic linkages; these features are most pronounced for Ca@CBC/β-CD, indicating successful immobilization of β-CD on the Ca-bearing carbon. Given the low N content of the samples, no distinct FT-IR bands can be reliably assigned to N-containing groups. Any weak N–H/C–N contribution, if present, is likely overlapped by the broad O–H stretching band around 3400 cm^{-1} and the strong C–O/C–O–C vibrations in the 1000–1200 cm^{-1} region. Therefore, the FT-IR spectra mainly reflect O-containing groups, carbonate species, and β-CD-related glycosidic functionalities.

XRD patterns (Fig. 2b) corroborate these assignments. CBC and CBC/β-CD display a broad hump at $2\theta \approx 20–30°$, characteristic of amorphous carbon. In contrast, Ca@CBC and Ca@CBC/β-CD exhibit sharp reflections that match calcite-type $CaCO_3$ (PDF#05–0586), while no characteristic peaks attributable to CaO or $Ca(OH)_2$ were detected. This indicates that $CaCO_3$ remained the predominant crystalline Ca phase after carbonization at 600 °C under N_2. The $CaCO_3$ phase persists after β-CD grafting, implying that microwave-assisted functionalization primarily alters the carbon surface chemistry while leaving the inorganic crystalline phase essentially unchanged. Collectively, the coexistence of $CaCO_3$-bearing domains and β-CD-derived oxygenated functionalities furnishes complementary sites for pollutant adsorption and complexation.

To directly evaluate the role of microwave irradiation in the β-CD grafting step, a comparative experiment was conducted using the same batch of Ca@CBC precursor and the same grafting formulation, while varying only the heating mode. As shown in Fig. S4, the microwave-assisted route required only 15 min, whereas the water-bath-heated route required 120 min to complete the same functionalization step. In parallel, the measured electricity consumption increased markedly from approximately 0.09 kWh for the microwave route to about 0.60 kWh for the water-bath route. Under standard adsorption conditions, the microwave-grafted sample also showed a higher adsorption capacity than the water-bath-heated counterpart. These results demonstrate that microwave irradiation is an efficient intensification strategy for β-CD functionalization in the present material system. The markedly reduced reaction time and electricity demand indicate clear time- and energy-saving advantages, while the moderately improved adsorption capacity suggests

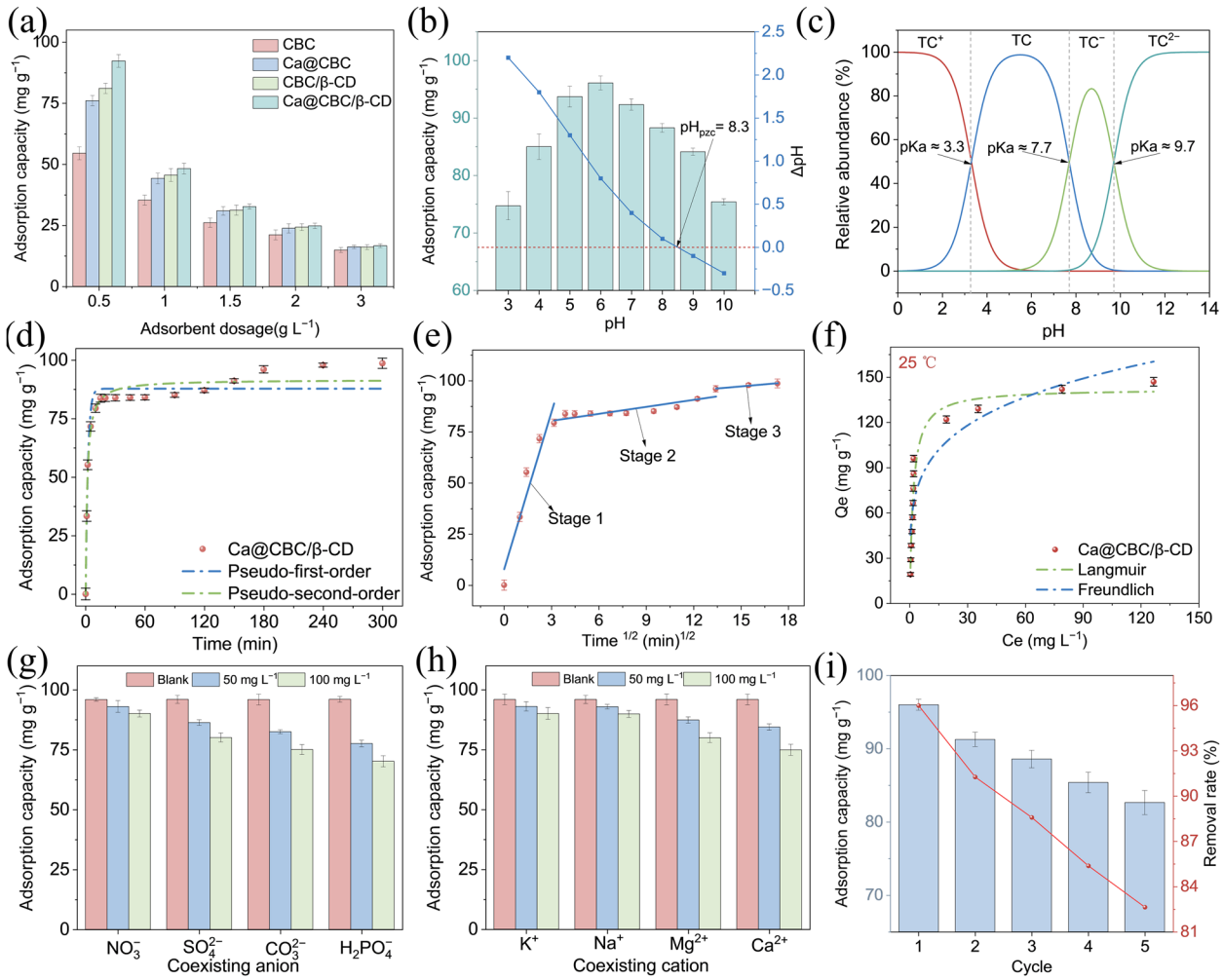

Fig. 3 Adsorption performance analysis of CBC-based adsorbents toward TC. **a** Impact of adsorbent dosage (pH = 5.0, t = 3 h, C_0 = 50 mg L^{-1}); **b** Effect of pH and ΔpH (dosage = 0.5 g L^{-1}, t = 3 h, C_0 = 50 mg L^{-1}); **c** TC speciation vs pH (pK_a = 3.3, 7.7, 9.7); **d** Adsorption kinetics of Ca@CBC/β-CD (pH = 6.0, dosage = 0.5 g L^{-1}, C_0 = 50 mg L^{-1}); **e** Pore diffusion model; **f** Adsorption isotherms models (pH = 6.0, dosage = 0.5 g L^{-1}, 25 °C); **g** Effect of coexisting anions; **h** Effect of coexisting cations; **i** Reusability over five adsorption–desorption cycles

more effective interfacial grafting and preservation of accessible binding domains. Because the Ca@CBC precursor was prepared by the same conventional carbonization route in both cases, the observed differences can be primarily attributed to the distinct heating modes used during β-CD immobilization rather than to variations in the initial biochar formation step.

3.2 Batch experiment results

The effect of adsorbent dosage on the equilibrium capacity is shown in Fig. 3a. At a C_0 of 50 mg L^{-1}, pH of 5.0, and a contact time (t) of 3 h, the Q_e monotonically decreased as the dose increased from 0.5 to 3.0 g L^{-1}. Notably, the performance consistently followed the order: Ca@CBC/β-CD > CBC/β-CD > Ca@CBC > CBC. This is because, at a fixed solute mass, an increased dose introduces an excess of active sites, leading to a reduced number of TC molecules adsorbed per unit mass. Concurrently, particle aggregation/masking and a thickened boundary layer decrease the proportion of accessible active sites and the external diffusion flux. While Q_e declines, the overall removal efficiency often increases with the dose, highlighting a trade-off between efficiency and economic viability. Therefore, a representative low dose of 0.5 g L^{-1} was selected for the subsequent experiment.

As shown in Fig. 3b, c, the point of zero charge (pH_{PZC}) of the material is approximately 8.3. The Q_e remained high in the pH range of 3–7 but dropped significantly at higher pH values. This can be explained by the speciation of TC, which is sensitive to pH. At pH ≈ 6, TC

primarily exists in forms that are favorable for both host–guest inclusion with β-CD and the formation of bridging/inner-sphere complexes with the material's functional groups and Ca^{2+} sites. Conversely, at high pH, electrostatic repulsion between the negatively charged adsorbent surface and anionic TC species intensifies, leading to a decrease in adsorption capacity (Zhao et al. 2012). This confirms that pH ≈ 6 is the optimal pH for TC adsorption on Ca@CBC/β-CD.

The adsorption kinetics, presented in Fig. 3d, show a rapid initial uptake followed by a slower approach to equilibrium over approximately 3 h. As detailed in Table S3, kinetic modeling revealed that the pseudo-second-order (PSO) model provided a better fit ($R^2 = 0.9755$) than the Pseudo-First-Order (PFO) ($R^2 = 0.9514$) model. This result indicates that the adsorption rate is primarily governed by chemical interactions and active site occupancy, as previously reported by Ho and McKay (Ho and McKay 1998). However, this empirical model is not able to predict changes in performance as a function of operating conditions. Therefore, the experimental conditionality of the PSO rate constant (k_2) can lead to erroneous conclusions when comparing literature results. Further analysis using the segmented Weber-Morris plot (Fig. 3e) confirmed a multi-stage process. The non-zero intercepts of each segment suggest that intra-particle diffusion is not the sole rate-limiting step. The overall process begins with film diffusion, transitions to intra-particle diffusion, and concludes with a reaction-coupled diffusion equilibrium. This complex behavior is consistent with the required conformational changes and interfacial reactions for both Ca^{2+}-mediated complexation and β-CD inclusion.

A comparison of Fig. 3f and Fig. S5 shows that, at pH 6.0 and a dosage of 0.5 g L^{-1}, the TC adsorption isotherms are better fitted by the Langmuir model than by the Freundlich model, implying approximately homogeneous sites with predominant monolayer coverage. As shown in Table S3, at 25 °C, Langmuir fitting yields $Q_{max} = 142.36$ mg g^{-1}, $K_L = 0.5839$ L mg^{-1} ($R^2 = 0.9605$), and the separation factor at $C_0 = 50$ mg L^{-1} is $R_L = 0.0331$, indicative of favorable adsorption. With increasing temperature, Q_{max} rises monotonically (142.36 → 153.11 → 161.91 mg g^{-1}, at 25 → 35 → 45 °C) and the Langmuir fit improves ($R^2 \approx 0.96 \rightarrow 0.98$), consistent with an endothermic character wherein desolvation and conformational matching promote Ca^{2+}-bridging/inner-sphere complexation and β-CD inclusion of TC (Wang et al. 2025). Although $n > 1$ for Freundlich, its overall fit and error are inferior to Langmuir, suggesting that multilayer/heterogeneous contributions are secondary.

The effect of coexisting ions is shown in Fig. 3g–h. The inhibitory order for anions was $H_2PO^{4-} > CO_3^{2-} > SO_4^{2-} > NO_3^-$. Phosphate ($H_2PO^{4-}$) readily forms sparingly soluble salts with Ca^{2+} and directly occupies Ca-sites. Carbonate (CO_3^{2-}) promotes $CaCO_3$ deposition and raises the pH, which weakens both inclusion and complexation. Sulfate (SO_4^{2-}) and nitrate (NO_3^-) primarily affect the outer-sphere adsorption by influencing ionic strength and electrical double-layer compression. On the cation side, the order was $Ca^{2+} > Mg^{2+} > Na^+ \approx K^+$. Divalent ions significantly reduced *Qe* through electrical double-layer compression and competitive complexation, with Ca^{2+} exhibiting the strongest inhibition due to a common ion effect. Monovalent ions had a weaker impact, mainly by altering the ionic strength. It is noteworthy that while the neutral cavity of β-CD is relatively unaffected by the valence of the ion, competition at the Ca^{2+} sites weakens the overall synergistic effect.

To further examine more realistic wastewater constituents, the effects of humic acid (HA) and trivalent cations were also evaluated (Fig. S6). Compared with the mono/divalent cations, HA, Fe^{3+}, and Al^{3+} caused a stronger suppression of TC uptake, and the apparent inhibitory order was $Fe^{3+} > Al^{3+} \approx$ HA. This behavior was mainly attributed to solution complexation with TC, competitive coordination with Ca-related active sites, and partial masking of accessible adsorption domains by organic or hydrolyzed metal species.

The regeneration performance of the material is shown in Fig. 3i. After five adsorption–desorption cycles using 0.1 M NaOH as the desorption agent, followed by washing with deionized water to near neutral pH, Ca@CBC/β-CD retained approximately 84–86% of its initial adsorption capacity. The alkaline treatment effectively desorbs most adsorbed TC by promoting deprotonation and weakening hydrogen bonding and Ca-mediated interactions. The remaining capacity loss is likely associated with three factors: (i) incomplete desorption of a small fraction of strongly bound or pore-embedded TC molecules; (ii) slight loss, masking, or passivation of Ca-containing active sites during repeated alkaline treatment; and (iii) partial passivation of β-CD-derived hydroxyl-rich sites, which may weaken the host–guest inclusion and hydrogen-bonding contribution upon cycling. Nevertheless, the retained capacity indicates that most of the Ca-related and β-CD-derived active sites remain effective after repeated regeneration.

To assess whether homogeneous Ca^{2+}–TC complexation in the bulk solution made a meaningful contribution, Ca leaching from Ca@CBC/β-CD was monitored under the optimum adsorption condition (Fig. S7). The dissolved Ca^{2+} concentration increased gradually with time, but remained low overall, rising only from ca. 0.05 mg L^{-1} at the initial stage to ca. 0.50 mg L^{-1} after 1440 min.

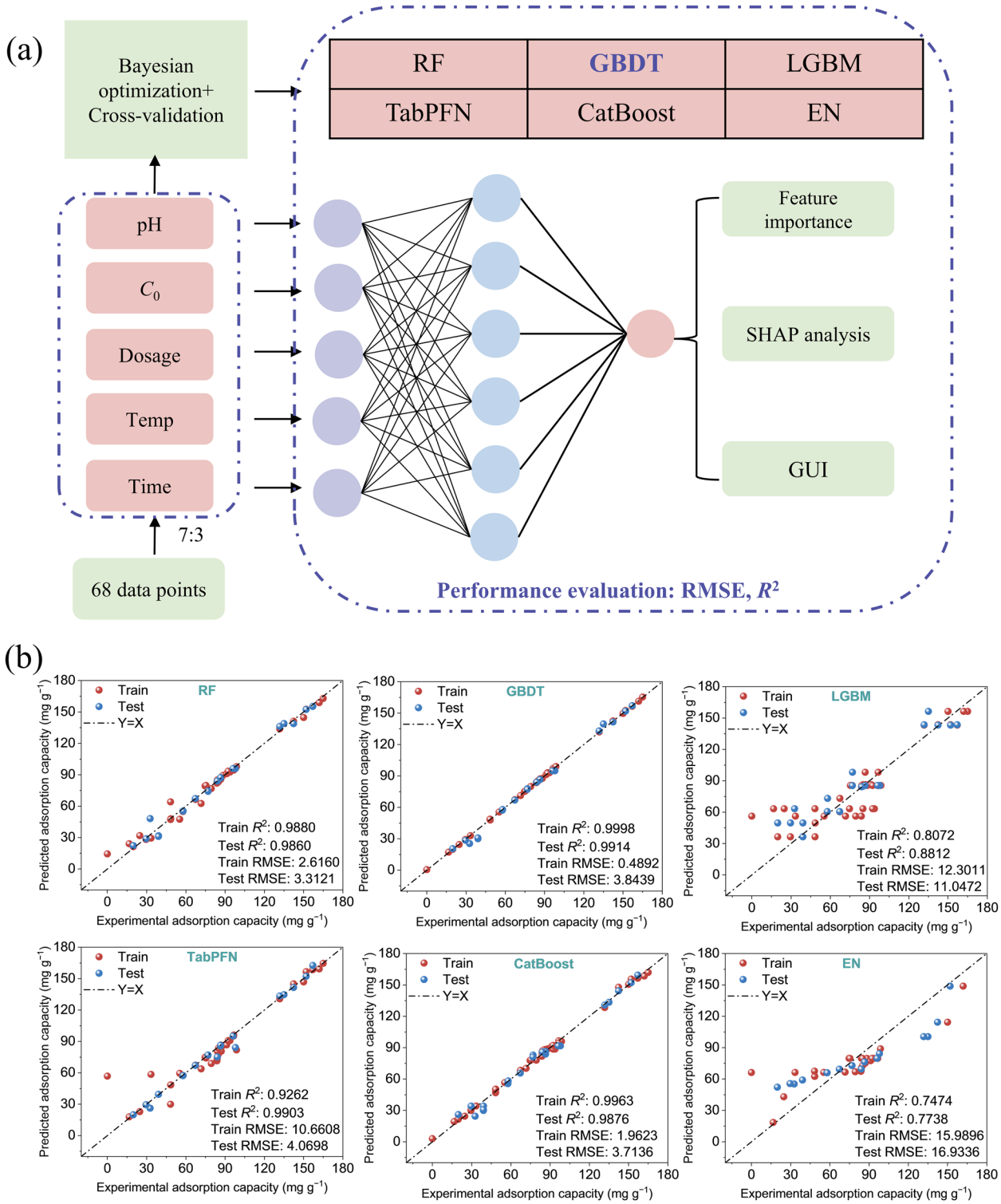

Fig. 4 **a** Machine learning workflow for predicting adsorption capacity and feature analysis. **b** Predicted vs. experimental adsorption capacity using six ML algorithms

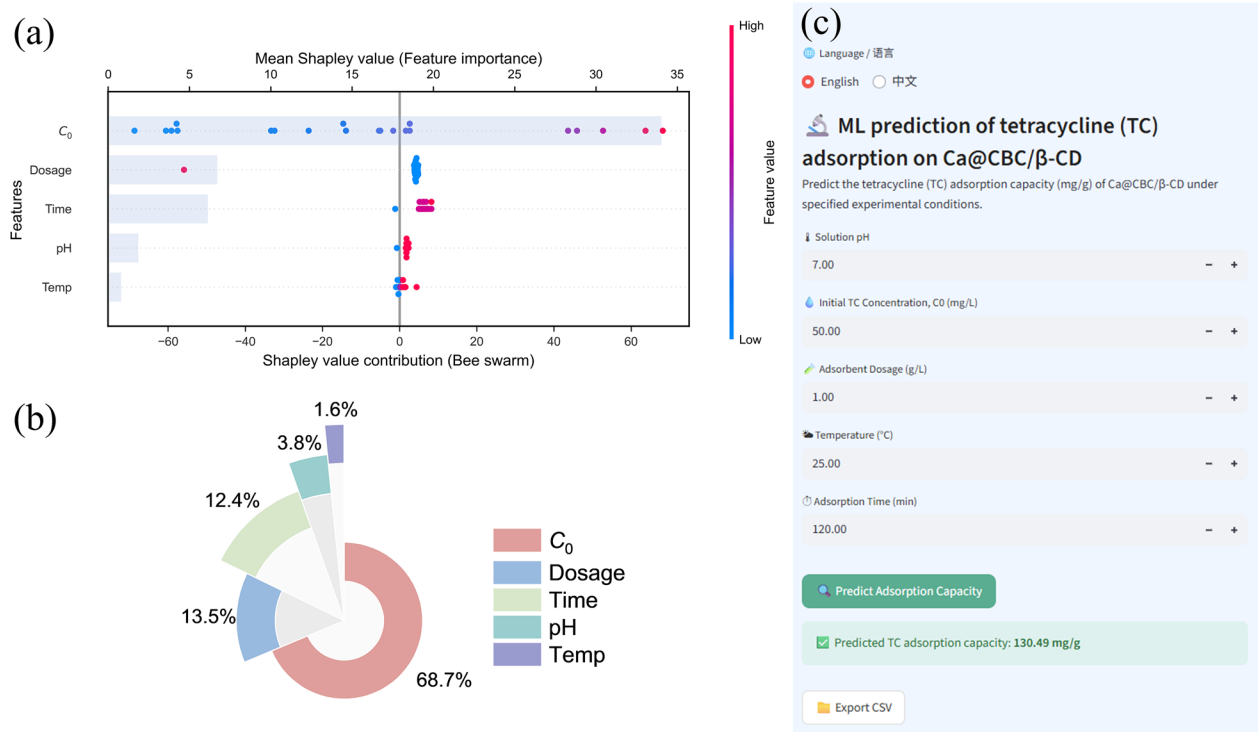

Fig. 5 SHAP analysis and model deployment of the GBDT model for predicting TC adsorption capacity. **a** SHAP summary plot showing feature impacts; **b** Donut chart illustrating feature importance; **c** Python-based GUI for interactive prediction using the optimized GBDT model

More importantly, within the equilibrium adsorption period used in this work (3 h), the dissolved Ca^{2+} level was still well below 1 mg L^{-1}. This indicates that only a small fraction of Ca was released into solution, whereas most Ca species remained anchored to the adsorbent surface. Accordingly, the dominant contribution of Ca is better described as surface-confined coordination/bridging at Ca-bearing domains, rather than homogeneous complexation by freely dissolved Ca^{2+} in the bulk phase. A minor contribution from leached Ca^{2+} at the solid–liquid interface cannot be ruled out, but it is unlikely to dominate the overall uptake pathway.

3.3 Machine learning results

As illustrated in Fig. 4a, the ML workflow integrates multifactorial input parameters (pH, C_0, dosage, temperature, and time), Bayesian hyperparameter optimization, and SHAP-based interpretability to predict adsorption capacity under complex experimental conditions. A total of 68 data points were divided into training and testing subsets at a 7:3 ratio. Six supervised algorithms were evaluated, including four tree-based ensemble methods (RF, GBDT, LGBM, CatBoost) and two non-tree baselines (EN and TabPFN). Although the dataset size is moderate, only five experimentally controlled input features were included, and Bayesian optimization with five-fold cross-validation was adopted to reduce the risk of overfitting. Moreover, overfitting was further assessed by comparing the R^2 and RMSE values of the training and testing sets. Table S2 presents the optimal hyperparameters for each ML model.

The parity plots in Fig. 4b reveal that most models achieved good predictive accuracy, with R^2 values above 0.95 for the training datasets. However, differences emerged in generalization ability on the testing datasets. Among the tree-based models, GBDT achieved the most consistent performance on the test dataset, with $R^2 = 0.9914$ and the lowest RMSE (3.8439 mg g^{-1}), clearly outperforming the other algorithms. In contrast, LGBM and EN exhibited a lower accuracy ($R^2 < 0.82$), reflecting their limited ability to capture nonlinear adsorption behavior with relatively small datasets. TabPFN performed competitively but did not surpass GBDT, while CatBoost and RF showed slightly higher variance between training and testing sets. The superior performance of GBDT can be attributed to three main factors: (1) Robust gradient boosting framework —GBDT sequentially builds trees to correct residual errors, which is particularly effective for small-to-medium datasets where subtle nonlinearities strongly influence the target variable; (2) Unlike RF, which grows many independent trees, GBDT optimizes each new tree to minimize

prediction errors, leading to smoother learning and improved generalization; (3) Compared with CatBoost and LGBM, GBDT is less sensitive to hyperparameter tuning and categorical handling, which may explain its stable behavior under limited experimental data conditions. Taken together, these findings confirm the superior robustness and generalization capability of GBDT, making it the most suitable model for further SHAP-based feature importance analysis and GUI implementation.

As illustrated in Fig. 5, the optimized GBDT model was further interpreted using SHAP to clarify the relative influence of each experimental factor. The SHAP summary plot (Fig. 5a) reveals the distribution of positive and negative contributions across different ranges of input variables, highlighting their nonlinear effects on TC adsorption. The feature importance donut chart (Fig. 5b) quantitatively demonstrates that the initial TC concentration (C_0) is the dominant predictor, accounting for 68.7% of the model's explanatory power. This strong influence can be explained by the fact that C_0 directly defines the driving force for mass transfer between solution and adsorbent, thereby governing adsorption kinetics. The next most influential variables are Dosage (13.5%) and adsorption Time (12.4%), which modulate adsorption capacity by altering the available surface sites and the extent of solute–sorbent interaction. In contrast, pH (3.8%) and Temperature (1.6%) exhibit weaker contributions, consistent with their secondary roles under the studied conditions.

In addition, a user-friendly Python-based GUI (Fig. 5c) was developed to integrate the trained GBDT model into an interactive prediction platform (source: https://ca-cbc-cdgui-3cg7fzpuezpteevvckxbyg.streamlit.app/). Through this interface, users can conveniently adjust experimental parameters (C_0, dosage, pH, temperature, and time) to obtain real-time predictions of TC adsorption capacity on Ca@CBC/β-CD. Such a tool not only facilitates the rational design of adsorption experiments but also demonstrates the practical utility of ML-assisted modeling for environmental remediation applications.

3.4 Structural characterization and adsorption mechanism

As shown in Fig. S8, the surface morphology of pristine Ca@CBC/β-CD changes markedly after TC adsorption. Before adsorption, the sample exhibits a hierarchical micro/nanostructure composed of Ca-rich particulates with open pore mouths. Following adsorption, abundant flocculent and particulate deposits uniformly coat the surface and bridge or locally occlude pore entrances, yielding a more compact appearance. The observed coverage and agglomeration suggest that TC preferentially accumulates at Ca sites and in proximity to β-CD cavities, likely forming a coordinative/inclusion "coating" that diminishes accessible porosity and edge sites. This morphological evolution aligns with the FT-IR/XPS results presented below, namely attenuation of carbonate bands, strengthened O–H hydrogen bonding, and enhanced inner-sphere Ca–O coordination.

It can be seen from Fig. 6 that the FT-IR spectra exhibit systematic changes upon adsorption. A stronger band emerges at ~ 1620 cm^{-1}, attributable to C = O and skeletal vibrations from TC, while the broad feature at ~ 3400 cm^{-1} (–OH stretching) further broadens and undergoes a slight red shift, indicating reinforcement of the hydrogen-bonding network between the surface and TC. The characteristic carbonate peaks of the support at 1420 cm^{-1} (ν_3) and 880 cm^{-1} (ν_2) are attenuated, reflecting surface coverage and a modified local coordination environment. The C–O–C signal of β-CD (~ 1348 cm^{-1}) remains discernible, consistent with stabilization via host–guest inclusion and interfacial hydrogen bonding.

XPS provides element-level corroboration (Fig. 6). The O 1 s envelope (Fig. 6b) can be deconvoluted into components at ~ 531.8–531.9 eV (C = O/M–O–C) and ~ 533.3–533.9 eV (C–O/–OH/–OH/H_2O). After adsorption, the area fraction of the lower-binding-energy component increases from 64.5% to 79.5% (≈10–20% absolute gain), directly evidencing the growth of inner-sphere Ca–O coordination (M–O–C) at the surface. In Ca 2p (Fig. 6c), the pre-adsorption peaks, $2p_{3/2}$ = 347.77 eV and $2p_{1/2}$ = 351.29 eV (Δ = 3.52 eV; $I_{1/2}$:$I_{3/2}$ ≈ 0.48), shift post-adsorption to 347.90/351.42 eV (Δ = 3.52 eV; $I_{1/2}$:$I_{3/2}$ ≈ 0.46). The spectrum shows only a modest positive shift (~ 0.13 eV) with essentially unchanged spin–orbit splitting and intensity ratio, indicating that Ca remains as Ca^{2+}, and that adsorption alters its coordination/coverage environment rather than its valence. After adsorption, N 1 s (Fig. 6d) resolves into three peaks at 398.14, 399.95, and 400.26 eV, assignable to coordination-related N (pyridinic/coordination-N), amine/amide-N, and weakly protonated/hydrogen-bonded N, respectively—consistent with hydrogen bonding and local coordination involving β-CD/surface –OH groups and TC. A four-component model best describes C 1 s (Fig. 6e): 284.8 eV (C–C/C = C), 285.6–286.2 eV (C–O/C–N), ~ 288.0 eV (C=O/amide), and ~ 289.3 eV (O–C = O/CO_3^{2-}). Following adsorption, the 286/288 eV components increase (coverage by β-CD/TC), whereas the ~ 289.3 eV carbonate component decreases, in agreement with the FT-IR changes at 1420/880 cm^{-1}.

From the analysis of FT-IR and XPS results, it emerges that the dominant mechanism at pH = 6, where neutral/zwitterionic TC prevails, comprises cooperative Ca^{2+}–O inner-sphere coordination and β-CD inclusion–hydrogen bonding, with π–π stacking and hydrophobic enrichment

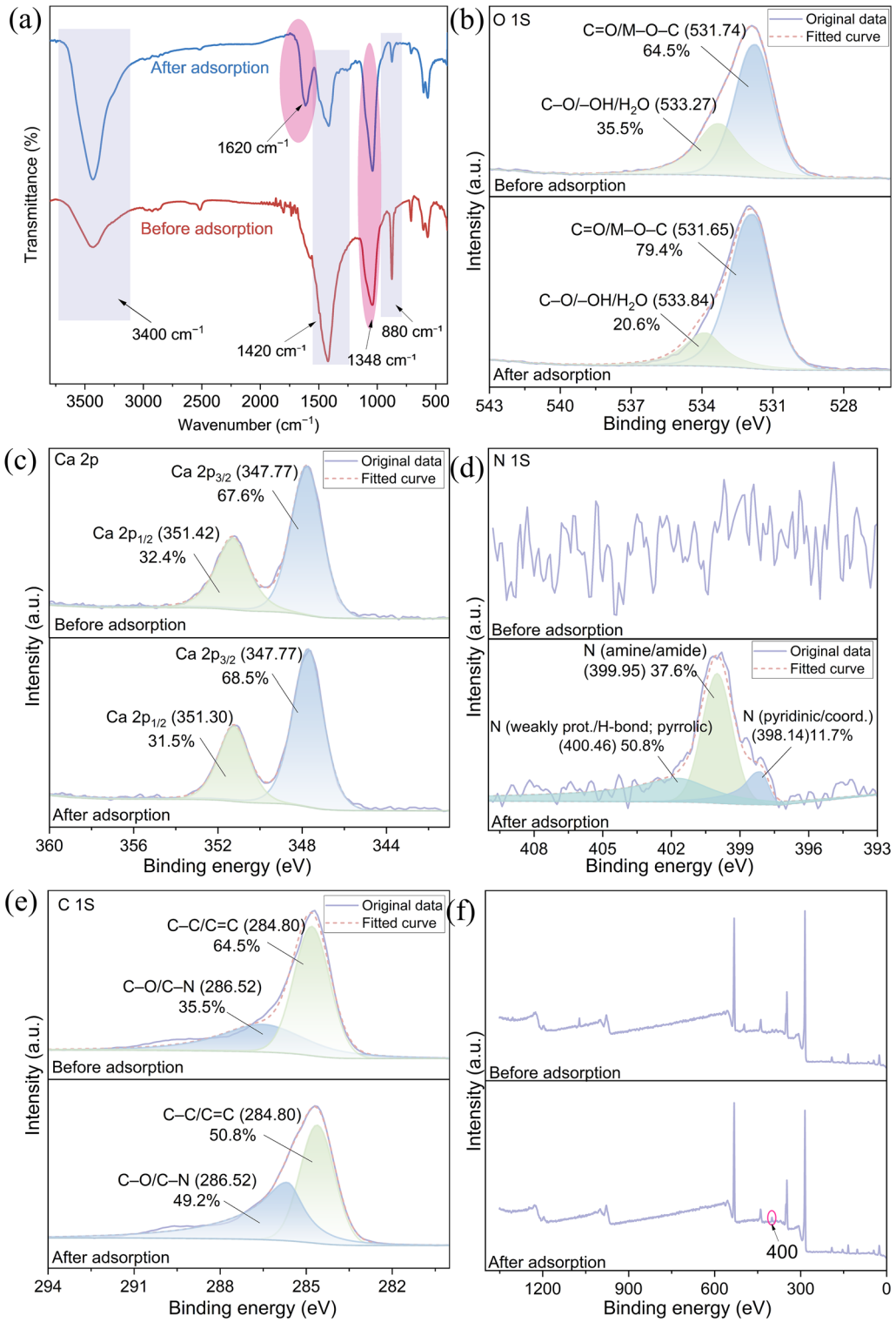

Fig. 6 FT-IR and XPS analyses of Ca@CBC/β-CD before and after TC adsorption. **a** FT-IR spectra; **b** O 1s; **c** Ca 2p; **d** N 1s; **e** C 1s; and **f** XPS full scan

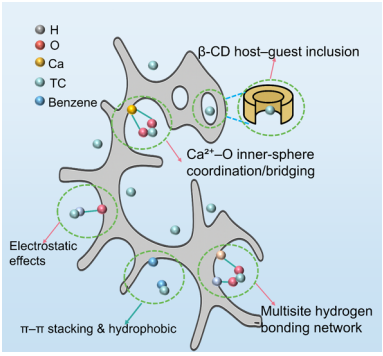

Fig. 7 Schematic diagram of the adsorption mechanism of TC on Ca@CBC/β-CD

providing secondary contributions (Fig. 7). The key chemical steps are summarized below:

a) Inner-sphere coordination

$$-O^{-}-Ca(H_2O)_n + TC(=O, O-H) \rightleftharpoons > O^{-}-Ca-O(TC) + n\,H_2O \quad (5)$$

b) Surface bridging with O, O′ chelation

$$-O^{-}-Ca^{2+}-O_{surf} + TC\left(O^{-}/C=O\right) \rightleftharpoons > O^{-}-Ca^{2+}-O(TC)-O'(TC) \quad (6)$$

c) β-CD host–guest inclusion

$$\beta\text{-CD} + TC \rightleftharpoons \beta\text{-CD} \supset TC \quad (7)$$

d) Multipoint hydrogen-bond network

$$-OH_{(\beta\text{-CD/surface})} + O=C-TC \rightleftharpoons —OH\cdots O=C-TC \quad (8)$$

e) π–π/hydrophobic enrichment

$$\text{graphitic } C(\pi) + TC(\pi) \rightleftharpoons C\pi\cdots\pi TC \quad (9)$$

f) Strong chelation by minor anionic TC species

$$Ca^{2+} + TC^{-} \rightleftharpoons Ca-TC\ (\text{inner}-\text{sphere chelate}) \quad (10)$$

It should be emphasized that reactions (5–6) align with the increased low-BE O 1 s component and invariant Ca 2p spin–orbit splitting. Reactions (7–8) rationalize the ~ 3400 cm^{-1} broadening/red shift and the N 1 s feature at ~ 400.3 eV. Reaction (9) accounts for the cooperative π–π/hydrophobic contribution to adsorption energy but does not produce a distinct signature in the XPS line shape.

Therefore, the co-modification strategy should be understood as complementary rather than competitive: Ca-bearing domains mainly govern coordination/bridging interactions, whereas β-CD provides inclusion and hydrogen-bonding interactions. This functional complementarity broadens the accessible adsorption pathways and underlies the superior performance of Ca@CBC/β-CD relative to the singly modified materials. Importantly, this synergy helps overcome the intrinsic limitation of Ca-modified biochar, namely its insufficient surface functionality. While Ca-bearing domains mainly contribute coordination/bridging sites, β-CD introduces inclusion cavities and hydroxyl-rich binding sites. Altogether, these two complementary mechanisms broaden the accessible adsorption pathways for TC.

3.5 Density functional theory (DFT) analysis

In Fig. 8a, electrostatic potential (ESP) maps reveal strong electrostatic complementarity: highly negative pockets on TC carbonyl/phenolate O oppose the strongly positive region around Ca on Ca@CBC, whereas the β-CD cluster presents alternating positive/negative patches around the outer rim that are predisposed to H-bonding. Frontier orbitals (Fig. 8b) show that the HOMO density resides mainly on the π-system of TC, whereas the LUMO density is available on Ca@CBC/β-CD, favoring electron donation from TC to the adsorption site upon coordination/H-bonding. The HOMO–LUMO gaps of the isolated building blocks (≈8.00, 7.21, and 2.68 eV for TC, Ca@CBC, and β-CD, respectively) suggest that β-CD is the most polarizable partner, while Ca@CBC remains the more electron-accepting site. Electron localization function (ELF) pictures (Fig. 8c) further indicate concentrated localization around heteroatoms and along the Ca center, consistent with the envisaged donor–acceptor contacts. These electronic features rationalize why chelating/anchoring modes (Conformation 1/Conformation 2) and the double-H-bonded outside-rim mode (Conformation 3) are the most chemically reasonable starting points, in line with the XPS/FT-IR indications of Ca–O coordination and H-bond formation.

To represent the elementary adsorption reactions summarized by Eqs. (5–10)—namely O,O′ chelation with surface participation, monodentate coordination assisted by a surface bridge, and outside-rim adhesion mediated by hydrogen bonding—we selected three optimized structures (Conformations 1–3) as prototypes of these motifs. In Fig. 9a, the IGMH δg_{inter}–sign(λ_2)ρ scatter plots and the corresponding colored δg_{inter} isosurfaces provide the interaction "fingerprints." Conformation 1 shows two compact blue/green basins between Ca and the two O donors together with an extended green contact at the TC–carbon interface, in line with the O,O′–Ca chelation plus surface anchoring envisaged in Eqs. (5, 6) and (9). Conformation 2 exhibits one dominant Ca–O basin

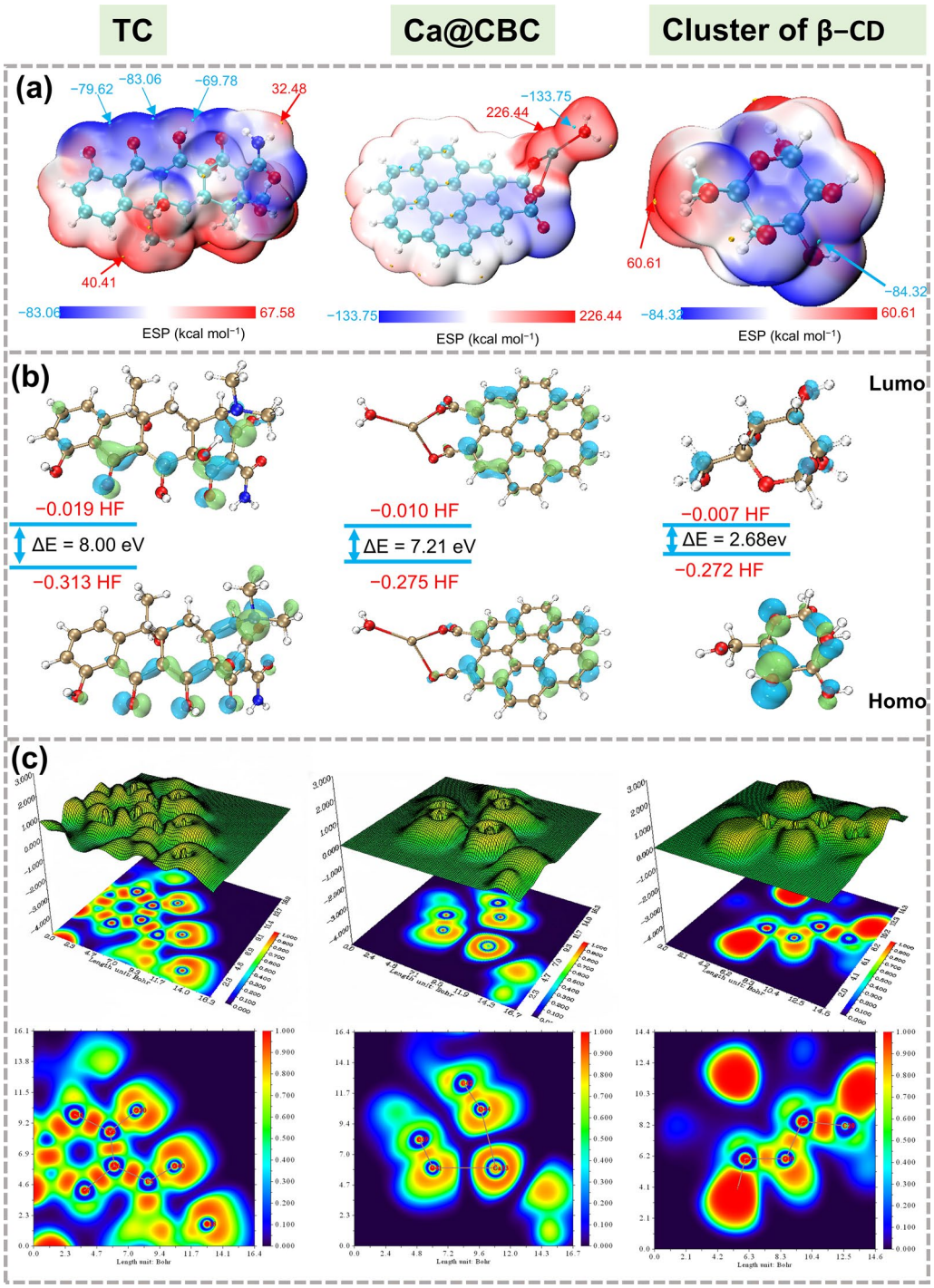

Fig. 8 **a** Electrostatic potential (ESP) surfaces (kcal mol^{-1}); **b** Frontier molecular orbitals (LUMO/HOMO) and HOMO–LUMO gaps (ΔE); **c** Electron localization function

and a continuous green strip that bridges TC to the carbon sheet, matching the monodentate coordination–anchoring-bridge motif in Eq. (5). Conformation 3 lacks Ca–O basins but displays two localized blue lobes at the β-CD rim and a broad outer-wall green region, consistent with the "outside-rim adhesion + double H-bonds" described by Eqs. (7–8).

The HS d_{norm} maps in Fig. 9b localize the closest contacts, while the 2D fingerprints quantify them. Conformation 1 presents multiple intense red patches and

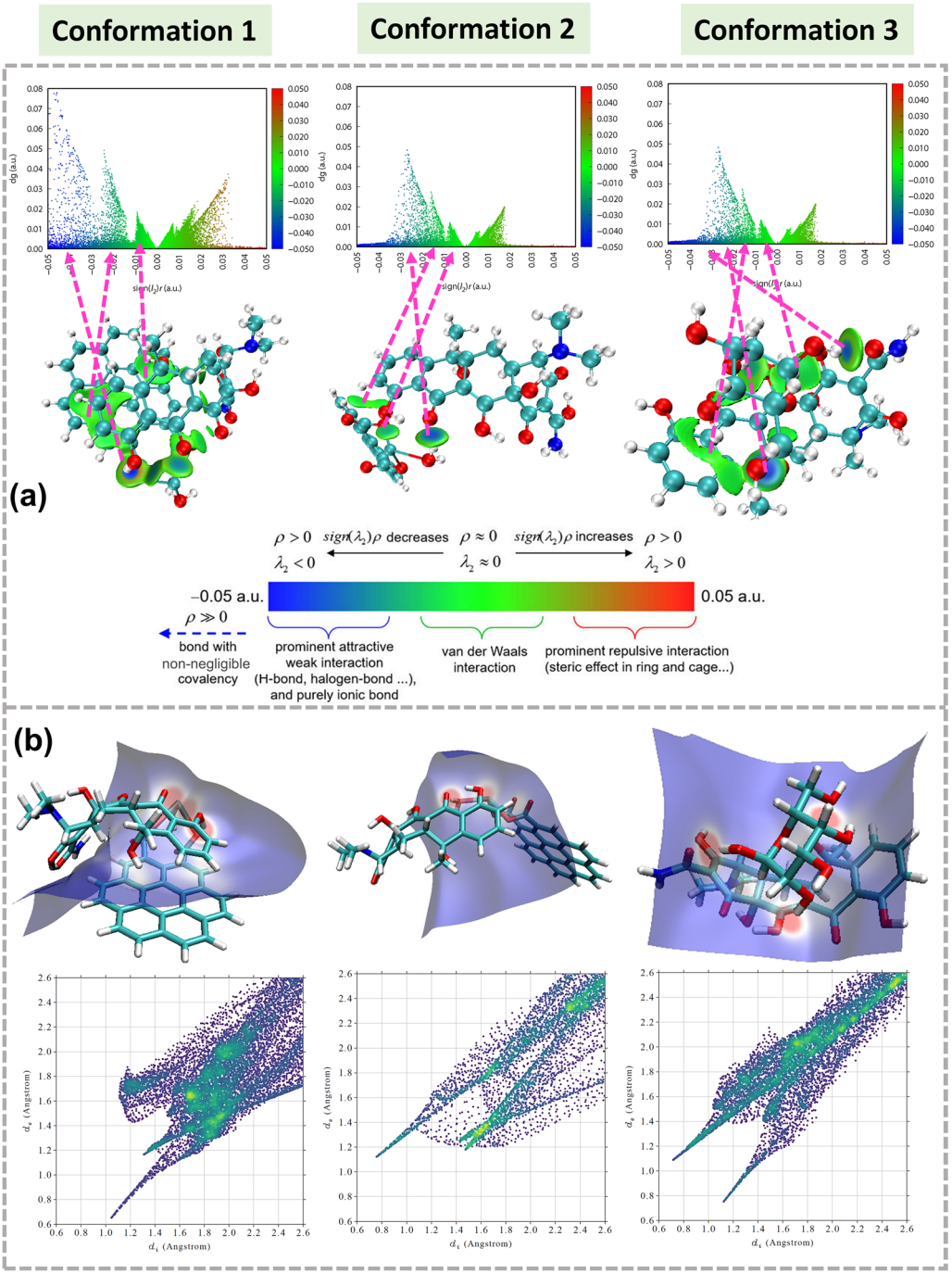

Fig. 9 IGMH and HS analyses diagnose the contact motifs in three optimized adsorption conformations

dense low-(d_i,d_e) spikes at the Ca···O/TC–surface sites, consistent with chelation plus surface contact. Conformation 2 shows a single prominent red patch/spike set for Ca···O together with an elongated wing that tracks the anchoring bridge to the carbon surface. Conformation 3 features two red patches at the β-CD rim and characteristic H-bond spikes, accompanied by a broad distribution attributable to outer-wall adhesion. These spatial signatures align with the spectroscopic observations: Ca–O coordination in Conformations 1–2 rationalizes the Ca 2p/O 1s shifts and the ν(C=O)/ν(C–O) redshifts in FT-IR, whereas Conformation 3 mainly

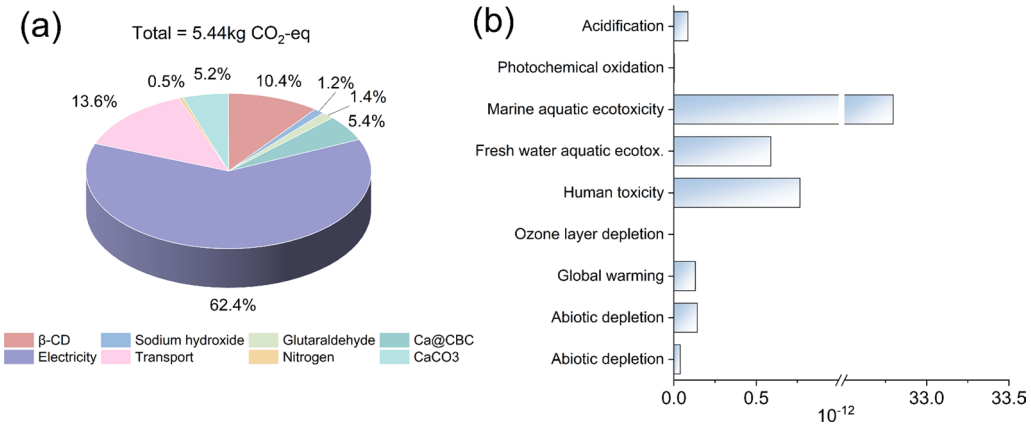

Fig. 10 Life cycle impacts of Ca@CBC/β-CD adsorbent in Stage 1: **a** contribution to GWP and **b** midpoint profile

perturbs O–H stretching and reorganizes the rim H-bond network without introducing a new Ca–O component in XPS.

3.6 Life cycle assessment results

In Fig. 10a, Stage 1 greenhouse gas emissions total 5.44 kg CO_2-eq. Electricity is the dominant hotspot (62.4%), driven primarily by tube-furnace heating/soak and the power demand of stirring and microwave units. Transport is second (13.6%), reflecting logistics for waste eggshells and other inputs. β-CD ranks third (10.4%). Sodium hydroxide and glutaraldehyde contribute 5.4% and 5.2%, respectively, indicating impacts associated with alkali production and organic crosslinking/functionalization. Nitrogen (0.5%) and material-related items ($CaCO_3$ and Ca@CBC, ≈2.6% combined) are minor. Overall, energy use and logistics dominate the preparation-stage carbon footprint, followed by β-CD, with alkali and the remaining organic reagents as smaller contributors.

The CML-IA midpoint profile in Fig. 10b is led by marine ecotoxicity, followed by human toxicity and freshwater ecotoxicity. An axis break highlights the orders-of-magnitude dominance of marine ecotoxicity. Photochemical oxidation and acidification are observable but smaller, while global warming, ozone depletion, and resource depletion contribute less. Toxicity-related burdens arise mainly from the electricity mix (coal share), NaOH from chlor-alkali production, and upstream inventories of glutaraldehyde/solvents; transport NO_x/VOC adds marginally to photochemical oxidation and acidification. Accordingly, measures to mitigate environmental burdens include: deploying renewable electricity and implementing heat integration/waste-heat recovery

Table 2 Comparison of maximum tetracycline adsorption capacities of different adsorbents under representative sorption conditions

Adsorbent	q_{max} (mg g^{-1})	Adsorption conditions	Ref.
Wheat straw biochar (Mn-BC)	107.77	C_0 = 100 mg L^{-1} (kinetics)/isotherms at 288–308 K; dosage = 1.0 g L^{-1}; 24 h; pH effect examined separately	Huang et al. (2023)
Iron- and manganese-oxides-loaded biochar (FeMn-BC-3)	14.24	C_0 = 40 mg L^{-1}; pH = 11; equilibrium capacity screened under alkaline condition	Zhang et al. (2021a)
Ball-milled wheat stalk biochar	84.54	Optimal pH ≈ 6–8; ball-milled biochar pyrolyzed at 600 °C; best reported adsorption amount	Xiang et al. (2020)
Ball-milled crayfish shell biochar (BCFS800)	60.70	C_0 = 100 mg L^{-1}; pH = 7.0; 20 °C; dosage = 1.25 g L^{-1}; 3 h	Zhang et al. (2021b)
Chitosan-based magnetic adsorbent (CS·Fe3O4)	211.21	pH = 7.0; 293 K; dosage = 0.5 g L^{-1}; C_0 varied from 10 to 200 mg L^{-1}	Silva et al. 2022)
Pharmaceutical-sludge activated biochar (BCD)	379.78	25 °C; broad pH adaptability; isotherm fitting reported at 15–35 °C	Liu et al. (2021)
Biochar-ceramsite composite (OBCC)	30.72	C_0 = 50–450 mg L^{-1}; 25 °C; dosage = 10.0 g L^{-1}; 24 h	Zhang et al. (2023a)
Modified alginate beads (PAM/CA@Cu)	356.57	pH ≈ 5.0; 30 °C; C_0 = 25–500 mg L^{-1}; isotherm experiments at 30 °C	Luo et al. (2021)
Ca@CBC/β-CD	161.91	pH = 6.0; dosage = 0.5 g L^{-1}; C_0 = 25–350 mg L^{-1}; 25–45 °C; 3 h	This study

to reduce energy intensity; improving β-CD grafting efficiency and ethanol recovery while evaluating greener crosslinkers or lowering glutaraldehyde usage; and optimizing local sourcing and transport routes to jointly reduce global warming potential and toxicity-related impacts.

3.7 Economic analysis and environmental impact

At laboratory scale, the cost of TC removal using Ca@CBC/β-CD was estimated within a direct operating cost (DOC) scope that includes only precursor inputs and utilities; labor, taxes, maintenance, and administrative overheads were excluded. Specifically, the DOC estimate included major reagents and utilities used during preparation, such as β-CD, glutaraldehyde, NaOH, N_2, electricity, and process water, while cotton stalk powder and eggshells were treated as waste-derived feedstocks with zero purchase cost. Table S5 summarizes that, when the functionalization dosage is optimized, the pyrolysis stage is well insulated with effective waste-heat recovery, and the feedstocks are primarily local waste biomass and by-product calcium sources, the unit direct cost of Ca@CBC/β-CD can be maintained at ≈\$1.2 kg^{-1}. Reported prices for commercial biochar span ~ \$0.449–1.847 kg^{-1}, situating the present Ca@CBC/β-CD within an acceptable range. The cost structure is jointly dominated by functionalization and energy use: β-CD grafting sets the overall cost level, while electricity consumption during pyrolysis is the second-largest contributor. Alkali, crosslinker, N_2, and process water are minor items. To sustain this cost range, three levers are recommended: (i) increase grafting efficiency and implement reagent recycling to further reduce the per-unit dosage of the functionalizing agent; (ii) continue to optimize furnace insulation, staged heating, and waste-heat reuse to lower specific energy consumption; and (iii) secure local supplies of waste feedstocks and by-product Ca sources to reduce variability at the feedstock end.

As summarized in Table 2, Ca@CBC/β-CD showed a relatively high TC adsorption capacity compared with several reported adsorbents. However, because these values were obtained under different experimental conditions, this comparison is intended only to provide a qualitative reference rather than a rigorous benchmark of adsorption performance. These results indicate that the present work achieves not only efficient enrichment of TC at the materials level, but also offers mechanistic and engineering value. Specifically, the host–guest recognition of β-CD, together with Ca^{2+}-mediated surface coordination/ion bridging, acts synergistically to confer broad adsorption affinity toward TC and structurally related antibiotics. In parallel, the biomass-derived scaffold and the straightforward impregnation/crosslinking route facilitate scale-up and shaping, with the potential to reduce specific treatment energy and operation-and-maintenance costs. Consequently, Ca@CBC/β-CD can serve as a high-performance, sustainable adsorption platform for antibiotic pollution control, providing a new materials option and design paradigm for the purification and management of complex real-world wastewaters.

4 Conclusion

In this study, a new β-CD modified calcium-rich biochar was described, characterized and studied for the adsorption of TC from wastewater. The reaction proposed was the crosslinking of β-CD onto CBC modified with waste eggshells as a Ca source (Ca@CBC/β-CD) via microwave assistance. Adsorption, mechanistic, ML, DFT calculations, and LCA data were discussed.

The proposed modification significantly enhanced the specific surface area and active sites of the material, leading to high-efficiency adsorption of TC. The adsorption isotherms were best fitted by the Langmuir model with a maximum adsorption capacity of 161.9 mg g^{-1}, while the kinetics followed the pseudo-second-order model. The optimal pH was found to be approximately 6. The adsorbent demonstrated resilience in the presence of multiple coexisting ions, maintaining approximately 84–86% of its capacity after five regeneration cycles. Mechanistically, the adsorption was dominated by the synergistic effects of Ca^{2+} inner-sphere complexation/bridging, β-CD host–guest inclusion, and hydrogen bonding, as mutually corroborated by spectroscopic analyses and DFT calculations. A ML comparison based on the experimental data revealed that the Gradient Boosting Decision Tree model performed most robustly (Test set $R^2 \approx 0.9914$), identifying initial concentration, adsorbent dosage, and contact time as key factors. A companion GUI was developed for rapid prediction and experimental design. Furthermore, an LCA revealed that the preparation stage resulted in greenhouse gas emissions of approximately 5.44 kg CO_2-eq kg^{-1}. Electricity consumption was identified as the primary environmental hotspot, suggesting that further impact reduction could be achieved by optimizing energy efficiency and reagent usage. Overall, Ca@CBC/β-CD demonstrates a combination of high efficiency, reusability, and relative sustainability, offering a promising material and pathway for the engineered adsorptive remediation of antibiotic-contaminated water, in line with the Sustainable Development Goals (SDGs). Beyond batch adsorption, Ca@CBC/β-CD also shows promise for future evaluation in continuous-flow fixed-bed column systems, which would provide a more application-relevant basis for assessing its engineering feasibility in practical wastewater treatment. Nevertheless, this study should be regarded as a proof-of-concept demonstration

under a fixed preparation route. Systematic optimization of the eggshell-to-cotton-stalk ratio, β-CD dosage, and microwave-assisted grafting conditions will be conducted in future work to further improve adsorption performance and support scale-up.

Supplementary Information

The online version contains supplementary material available at https://doi.org/10.1007/s42773-026-00640-w.

Supplementary material 1.

Acknowledgements
The first author, Chong Liu, would like to express his heartfelt gratitude to Prof. Fayong Li and Prof. Paramasivan Balasubramanian for their unwavering support, encouragement, and trust throughout this journey. He is also deeply grateful to Prof. Grégorio Crini and Prof. Ricardo Bello-Mendoza for their generous guidance, insightful advice, and invaluable help in the writing of this manuscript. The authors acknowledge the assistance of Instrumental Analysis Center of Tarim University.

Author contributions
Chong Liu: experiments, data curation, writing—original draft; Grégorio Crini: conceptualization, life-cycle assessment, writing—review and editing; Ricardo Bello-Mendoza: machine-learning modeling, DFT, writing—review and editing; Lee D. Wilson: methodology, characterization, supervision, writing—review and editing; Ali H. Jawad: experiments, data curation, writing—review and editing; Paramasivan Balasubramanian: experiments, characterization, writing—review and editing; Xuan Cuong Nguyen: machine-learning modeling, life-cycle assessment, visualization, writing—review and editing; Qingfu Zheng: characterization, validation, writing—review and editing; Fayong Li: conceptualization, methodology, supervision, funding acquisition, project administration, writing—review and editing. All authors read and approved the final manuscript.

Funding
This work was supported by the Science and Technology Program Project of Alaer City (2025GX06); Bingtuan Science and Technology Program (2024YD004; 2021DB019); President's foundation of Tarim University (TDZKCX202404), and earmarked fund for XJARS (XJARS-06).

Data availability
The Python codes used to build the models, raw data used in this study, model stable test results, and GUI application code are available at the following GitHub link (https://github.com/17609858895/Ca-CBC-CD).

Declarations

Competing interests
The authors declare that they have no known competing financial interests or personal relationships that could have appeared to influence the work reported in this paper.

Author details
[1]College of Water Hydraulic and Architectural Engineering, Tarim University, Xinjiang 843300, China. [2]Department of Chemical & Materials Engineering, University of Auckland, Auckland 1010, New Zealand. [3]Chrono-Environnement, Université Marie et Louis Pasteur, 25000 Besançon, France. [4]Department of Civil and Environmental Engineering, University of Canterbury, Private Bag 4800, Christchurch 8140, New Zealand. [5]Department of Chemistry, University of Saskatchewan, 110 Science Place, Room 165 Thorvaldson Bldg., Saskatoon, SK S7N 5C9, Canada. [6]Faculty of Applied Sciences, Universiti Teknologi MARA , 40450 Shah Alam, Selangor, Malaysia. [7]Environmental and Atmospheric Sciences Research Group, Scientific Research Center, Al-Ayen University, Thi-Qar, Nasiriyah 64001, Iraq. [8]Department of Biotechnology & Medical Engineering, National Institute of Technology Rourkela, Rourkela 769008, India. [9]Centre for Advanced Chemistry, Institute of Research and Development, Duy Tan University, Da Nang 550000, Vietnam. [10]Faculty of Environmental Chemical Engineering, Duy Tan University, Da Nang 550000, Vietnam. [11]College of Chemistry and Materials Science, Inner Mongolia Minzu University, Tongliao 028000, Inner Mongolia, China.

Received: 14 November 2025 Revised: 22 April 2026 Accepted: 1 June 2026
Published online: 02 July 2026

References

Antos J, Piosik M, Ginter-Kramarczyk D, Zembrzuska J, Kruszelnicka I (2024) Tetracyclines contamination in European aquatic environments: a comprehensive review of occurrence, fate, and removal techniques. Chemosphere 353:141519. https://doi.org/10.1016/j.chemosphere.2024.141519

Balasubramanian P, Prabhakar MR, Liu C, Zhang P, Li F (2024) Predictive capability of rough set machine learning in tetracycline adsorption using biochar. Carbon Res 3:48. https://doi.org/10.1007/s44246-024-00129-w

Chen Z, Lin B, Huang Y, Liu Y, Wu Y, Qu R, Tang C (2023) Pyrolysis temperature affects the physiochemical characteristics of lanthanum-modified biochar derived from orange peels: insights into the mechanisms of tetracycline adsorption by spectroscopic analysis and theoretical calculations. Sci Total Environ 862:160860. https://doi.org/10.1016/j.scitotenv.2022.160860

Chen M, Liu Y, Pan J, Jiang Y, Zou X, Wang Y (2024) Low-cost Ca/Mg co-modified biochar for effective phosphorus recovery: Adsorption mechanisms, resourceful utilization, and life cycle assessment. Chem Eng J 502:157993. https://doi.org/10.1016/j.cej.2024.157993

da Silva BF, Schnorr CE, da Rosa ST, Nunes FB, Baumann L, Müller EI, Silva LFO, Dotto GL, Bohn Rhoden CR (2022) Highly efficient adsorption of tetracycline using chitosan-based magnetic adsorbent. Polymers 14:4854. https://doi.org/10.3390/polym14224854

de Benedicto DFC, Ferreira GMD, Thomasi SS (2024) β-cyclodextrin-functionalized coffee husk biochar for surfactant adsorption. Colloids Surf, A 701:134921. https://doi.org/10.1016/j.colsurfa.2024.134921

Han X (2025) Efficient removal of lead ion from aqueous solution by β-Cyclodextrin modified magnetic sludge biochar. Biomass Conversion and Biorefinery 15:21107–21119. https://doi.org/10.1007/s13399-025-06721-3

Ho YS, McKay G (1998) A comparison of chemisorption kinetic models applied to pollutant removal on various sorbents. Process Saf Environ Prot 76:332–340. https://doi.org/10.1205/095758298529696

Huang Z, Fang X, Wang S, Zhou N, Fan S (2023) Effects of KMnO4 pre- and post-treatments on biochar properties and its adsorption of tetracycline. J Mol Liq 373:121257. https://doi.org/10.1016/j.molliq.2023.121257

Jiang W, Cai Y, Liu D, Shi Q, Wang Q (2023) Adsorption properties and mechanism of suaeda biochar and modified materials for tetracycline. Environ Res 235:116549. https://doi.org/10.1016/j.envres.2023.116549

Kayani KF (2025) Tetracycline in the environment: toxicity, uses, occurrence, detection, and removal by covalent organic frameworks – recent advances and challenges. Sep Purif Technol 364:132418. https://doi.org/10.1016/j.seppur.2025.132418

Khushbu JR (2022) β-Cyclodextrin mediated efficient removal of rose Bengal using chitosan/sodium alginate/graphene oxide nanocomposite: a comparative study. Iran Polym J 31:931–948. https://doi.org/10.1007/s13726-022-01053-9

Li C, Awasthi MK, Liu J, Yao T (2025) Veterinary tetracycline residues: environmental occurrence, ecotoxicity, and degradation mechanism. Environ Res 266:120417. https://doi.org/10.1016/j.envres.2024.120417

Liao Q, Rong H, Zhao M, Luo H, Chu Z, Wang R (2022) Strong adsorption properties and mechanism of action with regard to tetracycline adsorption of double-network polyvinyl alcohol-copper alginate gel beads. J Hazard Mater 422:126863. https://doi.org/10.1016/j.jhazmat.2021.126863

Liu H, Xu G, Li G (2021) Preparation of porous biochar based on pharmaceutical sludge activated by NaOH and its application in the adsorption of tetracycline. J Colloid Interface Sci 587:271–278. https://doi.org/10.1016/j.jcis.2020.12.014

Liu C, Balasubramanian P, Li F, Huang H (2024a) Machine learning prediction of dye adsorption by hydrochar: Parameter optimization and experimental

validation. J Hazard Mater 480:135853. https://doi.org/10.1016/j.jhazmat.2024.135853
Liu C, Bolan N, Rajapaksha AU, Wang H, Balasubramanian P, Zhang P, Nguyen XC, Li F (2024b) Critical review of biochar for the removal of emerging inorganic pollutants from wastewater. Chin Chem Lett. https://doi.org/10.1016/j.cclet.2024.109960
Liu C, Crini G, Wilson LD, Balasubramanian P, Li F (2024c) Removal of contaminants present in water and wastewater by cyclodextrin-based adsorbents: A bibliometric review from 1993 to 2022. Environ Pollut 348:123815. https://doi.org/10.1016/j.envpol.2024.123815
Liu C, Balasubramanian P, Nguyen XC, An J, Praneeth S, Zhang P, Huang H (2025a) Enhanced machine learning prediction of biochar adsorption for dyes: parameter optimization and experimental validation. Carbon Res 4:46. https://doi.org/10.1007/s44246-025-00213-9
Liu C, An J, Nguyen XC, Balasubramanian P (2025b) Machine learning prediction of hydrochar adsorption capacity for methylene blue with limited data: inspired by generative adversarial network-based augmentation. Energy & Environmental Sustainability 1:100043. https://doi.org/10.1016/j.eesus.2025.100043
Liu C, Balasubramanian P, An J, Li F (2025c) Machine learning prediction of ammonia nitrogen adsorption on biochar with model evaluation and optimization. Npj Clean Water 8:1–12. https://doi.org/10.1038/s41545-024-00429-z
Lu T (2024) A comprehensive electron wavefunction analysis toolbox for chemists, Multiwfn. J Chem Phys 161:082503. https://doi.org/10.1063/5.0216272
Lu T, Chen F (2012) Multiwfn: a multifunctional wavefunction analyzer. J Comput Chem 33:580–592. https://doi.org/10.1002/jcc.22885
Luo H, Liu Y, Lu H, Fang Q, Rong H (2021) Efficient adsorption of tetracycline from aqueous solutions by modified alginate beads after the removal of Cu(II) ions. ACS Omega 6:6240–6251. https://doi.org/10.1021/acsomega.0c05807
Nie Y, Zhao C, Zhou Z, Kong Y, Ma J (2023) Hydrochloric acid-modified fungi-microalgae biochar for adsorption of tetracycline hydrochloride: performance and mechanism. Bioresour Technol 383:129224. https://doi.org/10.1016/j.biortech.2023.129224
Qu J, Dong M, Wei S, Meng Q, Hu L, Hu Q, Wang L, Han W, Zhang Y (2020) Microwave-assisted one pot synthesis of β-cyclodextrin modified biochar for concurrent removal of Pb(II) and bisphenol a in water. Carbohydr Polym 250:117003. https://doi.org/10.1016/j.carbpol.2020.117003
Qu J, Dong M, Bi F, Tao Y, Wang L, Jiang Z, Zhang G, Zhang B, Zhang Y (2022) Microwave-assisted one-pot synthesis of β-cyclodextrin modified biochar for stabilization of Cd and Pb in soil. J Clean Prod 346:131165. https://doi.org/10.1016/j.jclepro.2022.131165
Qu J, Li Y, Sun H, Liu R, Han Y, Bi F, Fan H, Zhang G, Zhang Y, Wang Y, Cao W, Zhang Y (2024) Ball-milled sepiolite/phosphate rock for simultaneous remediation of cadmium-contaminated farmland and alleviation of phosphorus deficiency symptoms in pepper. Chem Eng J 488:150925. https://doi.org/10.1016/j.cej.2024.150925
Sanni SO, Oluokun O, Akpotu SO, Pholosi A, Pakade VE (2024) Removal of tetracycline from the aquatic environment using activated carbon: A comparative study of adsorption performance based on the activator agents. Heliyon. https://doi.org/10.1016/j.heliyon.2024.e34637
Shi Q, Wang W, Zhang H, Bai H, Liu K, Zhang J, Li Z, Zhu W (2023) Porous biochar derived from walnut shell as an efficient adsorbent for tetracycline removal. Bioresour Technol 383:129213. https://doi.org/10.1016/j.biortech.2023.129213
Tian B, Hua S, Tian Y, Liu J (2021) Cyclodextrin-based adsorbents for the removal of pollutants from wastewater: a review. Environ Sci Pollut Res 28:1317–1340. https://doi.org/10.1007/s11356-020-11168-2
Urooj T, Mishra M, Pandey S (2024) Unlocking environmental solutions: a review of cyclodextrins in pollutant removal. Discov Environ 2:65. https://doi.org/10.1007/s44274-024-00090-w
Wang W, Kong H, Wang J, Zhang G, Shen F, Liu F, Huang Z (2024) Lanthanum-calcium bimetallic-modified attapulgite- chitosan hydrogel beads for efficient phosphate removal from water: Performance evaluation, mechanistic and life cycle assessment. Carbohydr Polym 338:122183. https://doi.org/10.1016/j.carbpol.2024.122183
Wang S, Wang M, Wu H, Sun X, Dong Z, Peng W, Zhang B, Cai C, Qu J (2025) Microwave-assisted synthesis of a β-cyclodextrin/TEMPO-oxidized cellulose/Fe3O4 adsorbent for Pb and Cu remediation in soil. J Clean Prod 495:145100. https://doi.org/10.1016/j.jclepro.2025.145100
Xiang W, Wan Y, Zhang X, Tan Z, Xia T, Zheng Y, Gao B (2020) Adsorption of tetracycline hydrochloride onto ball-milled biochar: Governing factors and mechanisms. Chemosphere 255:127057. https://doi.org/10.1016/j.chemosphere.2020.127057
Xu J, Zhang Y, Li B, Fan S, Xu H, Guan D-X (2022) Improved adsorption properties of tetracycline on KOH/KMnO4 modified biochar derived from wheat straw. Chemosphere 296:133981. https://doi.org/10.1016/j.chemosphere.2022.133981
Zhang X, Li Y, Wu M, Pang Y, Hao Z, Hu M, Qiu R, Chen Z (2021a) Enhanced adsorption of tetracycline by an iron and manganese oxides loaded biochar: Kinetics, mechanism and column adsorption. Bioresour Technol 320:124264. https://doi.org/10.1016/j.biortech.2020.124264
Zhang D, He Q, Hu X, Zhang K, Chen C, Xue Y (2021b) Enhanced adsorption for the removal of tetracycline hydrochloride (TC) using ball-milled biochar derived from crayfish shell. Colloids Surf Physicochem Eng Asp 615:126254. https://doi.org/10.1016/j.colsurfa.2021.126254
Zhang K, Zhang L, Dong X, Zhao Y, Li F, Cen Q (2023a) Efficient adsorption of tetracycline hydrochloride on biochar-ceramsite composite: optimization of response surface methodology and investigation of adsorption mechanism. Materials Today Sustainability 24:100525. https://doi.org/10.1016/j.mtsust.2023.100525
Zhang P, Liu C, Lao D, Nguyen XC, Paramasivan B, Qian X, Inyinbor AA, Hu X, You Y, Li F (2023b) Unveiling the drives behind tetracycline adsorption capacity with biochar through machine learning. Sci Rep 13:11512. https://doi.org/10.1038/s41598-023-38579-8
Zhao Y, Gu X, Gao S, Geng J, Wang X (2012) Adsorption of tetracycline (TC) onto montmorillonite: Cations and humic acid effects. Geoderma 183–184:12–18. https://doi.org/10.1016/j.geoderma.2012.03.004
Zhuo S-N, Dai T-C, Ren H-Y, Liu B-F (2022) Simultaneous adsorption of phosphate and tetracycline by calcium modified corn stover biochar: Performance and mechanism. Bioresour Technol 359:127477. https://doi.org/10.1016/j.biortech.2022.127477